Plasma Sources Science and Technology

PAPER

Modeling of high pressure arc-discharge with a fully-implicit Navier–Stokes stabilized finite element flow solver

To cite this article: A Sahai *et al* 2017 *Plasma Sources Sci. Technol.* **26** 055012

IOP Publishing Plasma Sources Science and Technology
Plasma Sources Sci. Technol. **26** (2017) 055012 (21pp) https://doi.org/10.1088/1361-6595/aa638b

Modeling of high pressure arc-discharge with a fully-implicit Navier–Stokes stabilized finite element flow solver

A Sahai[1], N N Mansour[2], B Lopez[1] and M Panesi[1]

[1] University of Illinois at Urbana-Champaign, Urbana, Illinois 61801, United States of America
[2] NASA Ames Research Center, Moffett Field, California 94035, United States of America

E-mail: mpanesi@illinois.edu

Received 30 September 2016, revised 1 February 2017
Accepted for publication 28 February 2017
Published 3 April 2017

Abstract

This work addresses the modeling of high pressure electric discharge in an arc-heated wind tunnel. The combined numerical solution of Poisson's equation, radiative transfer equations, and the set of Favre-averaged thermochemical nonequilibrium Navier–Stokes equations allows for the determination of the electric, radiation, and flow fields, accounting for their mutual interaction. Semi-classical statistical thermodynamics is used to determine the plasma thermodynamic properties, while transport properties are obtained from kinetic principles with the Chapman–Enskog method. A multi-temperature formulation is used to account for thermal non-equilibrium. Finally, the turbulence closure of the flow equations is obtained by means of the Spalart–Allmaras model, which requires the solution of an additional scalar transport equation. A Streamline upwind Petrov–Galerkin stabilized finite element formulation is employed to solve the Navier–Stokes equation. The electric field equation is solved using the standard Galerkin formulation. A stable formulation for the radiative transfer equations is obtained using the least-squares finite element method. The developed simulation framework has been applied to investigate turbulent plasma flows in the 20 MW Aerodynamic Heating Facility at NASA Ames Research Center. The current model is able to predict the process of energy addition and re-distribution due to Joule heating and thermal radiation, resulting in a hot central core surrounded by colder flow. The use of an unsteady three-dimensional treatment also allows the asymmetry due to a dynamic electric arc attachment point in the cathode chamber to be captured accurately. The current work paves the way for detailed estimation of operating characteristics for arc-heated wind tunnels which are critical in testing thermal protection systems.

Keywords: arcjet, finite element, SUPG, Joule heating, radiation, arc attachment

1. Introduction

Plasma discharges have a wide range of applications, which include material processing, space propulsion, fuel conversion, green energy production, and plasma generation for the testing of thermal protection materials. The analysis presented here focuses on the study of plasma generated by high pressure arc discharges used in simulating high speed atmospheric entry.

Spacecraft and their payload are protected from the harsh environment encountered during the planetary entry at hypersonic speeds by thermal protection systems (TPS). In order to design reliable TPS, the heat loads need to be accurately characterized. Traditionally, this has been achieved through extensive wind tunnel testing using arc-jets, which are capable of generating high enthalpy flows with realistic temperature levels and heating rates [1]. In arc-jet facilities, a mixture of cold gas, representative of the planetary atmosphere, is injected into the constrictor. The high currents then lead to gas heating due to the Joule dissipation process. As the temperature increases, atoms and molecules ionize, and form a quasi-neutral plasma. The heated gas is subsequently

accelerated in a converging–diverging nozzle, before entering the test section. The fast acceleration imparted to the flow drives the gas out of equilibrium, causing several undesirable effects in the testing of models. Thus, an accurate description of the state of the gaseous mixture at the nozzle outlet is of paramount importance for characterizing the material testing process.

The objective of this work is to develop a three dimensional, unsteady, multi-physics simulation framework for accurately capturing the flowfield inside the Aerodynamic Heating Facility (AHF) arc heater located at NASA Ames Research Center [2]. Simulating the AHF is extremely challenging since it requires modeling the coupled problems of heating due to the electric discharge, energy redistribution through radiative transfer, and flow of chemically reactive plasma in the facility. Given the complexity of this calculation, the current analysis is restricted to the flow in the constricted-arc heater section, i.e. through the anode, cathode, and constrictor regions. Future work will address the modeling in the entire facility and would include the nozzle section and the test chamber.

Previous numerical studies of the AHF facility were carried out by Sakai *et al* [3–5] and Lee *et al* [6]. In these papers, the authors discuss the impact of radiation and turbulence on the plasma properties using a simple three band-radiation model, developed by Sakai and Olejniczak [3, 5], and a two-equation turbulence model. Similar analyses have been performed on the Kyushu University Wind Tunnel and on a larger arc heater in JAXA [7]. The main objective was to examine the impact of turbulent and radiative heat transfer on the flow-field for facilities of different sizes [8–11]. Trelles *et al* [12–15] have worked extensively on finite element modeling of industrially-relevant argon based arc plasma torches while employing simple empirical radiation models. These industrial torches, although similar in principle to arc-heated wind tunnels, are much smaller in size. Consequently, the research of Trelles *et al* has been focused on smaller geometries and lower values (10–100 kW [14]) of total power as compared to the AHF ($\sim$20 MW [16]).

Despite the axisymmetry of the geometry and boundary conditions, the flow in arc-heaters is inherently three-dimensional and time-dependent. These effects were not accounted for in any of the previous analyses on the AHF and arc-heated wind tunnels in general, which consider the flow as axisymmetric and steady. Furthermore, previous studies adopted a crude model for the description of the spectral properties of the plasma and the transport of radiation. This research is motivated by the need to promote a better understanding of the dynamics of the electromagnetic discharge in arc-jet facilities, which would ultimately allow a more accurate characterization of the plasma jet used in material testing. To this aim, a set of new physical models have been built upon the fully-implicit Navier–Stokes (FIN-S) flow solver [17, 18]. FIN-S is a state-of-the-art, parallel, adaptive, unstructured, finite element solver based on the LIBMESH library [19]. The wealth of physical processes occurring in the plasma discharge has required the implementation of additional models in the code to account for: (a) non-equilibrium effects in the gaseous mixture, (b) transport of energy due to thermal radiation, (c) and interaction with the electric field.

While the assumption of local thermodynamic equilibrium (LTE) may be well-justified in the smooth, low-speed flow inside the constrictor chamber, the steep gradients due to the strong acceleration in the nozzle may cause substantial deviations from equilibrium. Since the long term goal of this analysis is to provide a complete description of the flow in the entire facility, non-equilibrium effects have been included in the analysis. Over the last few decades several non-equilibrium models have been developed [20–22]. The current work uses the two temperature formulation developed by Park [23, 24]. The two temperature model model requires the numerical solution of the Navier–Stokes equations complemented by additional equations expressing the conservation of the individual chemical components in the gas, and the energy of the internal degrees of freedom of atoms and molecules [25]. Thus, the closure of this system of equations requires the knowledge of chemical reaction rate source terms, non-equilibrium energy transfer source terms, and the characterization of the thermodynamic properties and transport fluxes. In this work, semi-classical statistical mechanics has been used to describe the thermodynamic properties of the plasma [26], while the transport properties have been obtained from kinetic principles, with the method of Chapman and Enskog [27–29].

The determination of the radiation field in the arc-heater requires characterization of the spectral properties of the plasma and subsequently, a solution of radiation transfer equations (RTEs). A large number of numerical methods have become available in recent years for calculation of the radiative heat transfer in participating media. They can be broadly classified into: (a) techniques based on ray tracing, such as the ray tracing method [30, 31] and the Monte Carlo method [32, 33]; (b) and methods based on spatial discretization of the radiative transport equations like discrete ordinate methods [34], finite volume method [35], and finite element method [36]. The first category of methods, although numerically stable and more intuitive, is often time consuming, even for simple problems, and harder to implement in a parallel framework for complicated geometries. Therefore, the second class of methods has received considerable attention for performing radiation calculations in multi-dimensional domains. In this work, modeling of radiation has been performed by means of the discrete ordinate method. The most accurate approach to radiation modeling would entail solving the RTE in a given direction of propagation for a broad wavelength range, which characterize the spectrum of the plasma. Unfortunately, this approach is computationally expensive, and spectral models have to be used to make the problem tractable. Efficient radiation models like the band models [5, 37, 38], full-spectrum k-distribution model [39], and the multiscale k-distribution model [40] have been developed to overcome the computational challenges of line-by-line spectral integration. Although each of these approaches have yielded interesting results, their application has been limited to simplified symmetric flow-fields.

Finally, the evolution of the electromagnetic (EM) field requires the solution of the Maxwell's equations. There are different studies on the use of finite element discretization to solve the magneto-hydrodynamics equations [41, 42] which allow for the interaction between electromagnetic forces and the underlying flowfield to be resolved acccurately. The current analysis follows the approach adopted by researchers investigating the AHF and large arc-heated wind tunnels in general [5, 11] and introduces certain simplifications to the treatment of the EM field. The external and self-induced magnetic fields are neglected and electric discharge is modeled assuming a static electric field. Thus, the set of Maxwell's equations is replaced by the simpler Poisson's formulation, which allows for the determination of the electrostatic potential via the solution of a second-order differential equation, loosely coupled with the Navier–Stokes and RTE equations.

The paper is organized as follows: section 2 presents the physical model used in the current investigation, section 3 describes the numerical model applied to solve the governing equations, and section 4 discusses results obtained using the new framework. The conclusions are summarized in section 5.

2. Mathematical model: non-equilibrium plasma flows

A complete analysis of non-equilibrium arc-jet plasma flows should include the study of gas-dynamics, radiation and electromagnetic fields. Non-equilibrium reacting flows must satisfy a set of laws expressing the conservation of the species mass, momentum, total energy, and the energies associated with the internal degrees of freedom of the particles in the gas. At high temperatures, thermal radiation becomes an efficient mechanism of energy transport, and its contribution must be included in the mathematical model. This is done by solving the RTE coupled with the flow governing equations. Furthermore, at temperatures close to 10^4 K, the gas becomes ionized and electromagnetic fields play a major role in determining the dynamics of the system, thus requiring the solution of Maxwell's equations. The plasma is assumed to fulfill the following assumptions:

(1) The gas is composed of eleven chemical components defined by the set $\mathcal{S} = \{N_2, O_2, NO, N, O, N_2^+, O_2^+, NO^+, N^+, O^+, \text{and } e^-\}$. For convenience, $\mathcal{S}$ is further divided into the set of heavy particles $\mathcal{H}$ such that $\mathcal{S} = \mathcal{H} + \{e^-\}$.
(2) The plasma is considered quasi-neutral, since the Debye length is smaller than the characteristic flow length scale.
(3) Rotational and translational energy states are assumed to be in thermal equilibrium at a single *rotational-translational* temperature, T.
(4) Free-electrons, vibrational and electronic energies are assumed to be in thermal equilibrium with each other at an *electro-vibrational* temperature T_{ev} distinct from T.
(5) The effects of Lorentz force, Hall current, and ion slip are ignored.

The high pressures encountered in the arc-heater facility result in a large number of collisions and rapid thermal equilibration. Similar findings have been reported in previous studies focusing on the flow-field inside large arc-heated wind tunnels [5, 11]. Consequently, T_{ev} and T are expected to be in equilibrium in the majority of the flowfield. The impact of thermal non-equilibrium will become significant in the converging–diverging section of the nozzle. However, since this region of the arc-jet will be modeled in future studies, non-equilibrium effects have been accounted for in the current work in order to ease later comparative analysis.

2.1. Hydrodynamic equations: two temperature model

The species mass, mixture momentum, mixture total energy and vibronic energy conservation equations governing the dynamics of non-equilibrium plasmas are summarized below:

$$\partial_t \rho_i + \nabla \cdot [\rho_i(\mathbf{u} + \boldsymbol{\mathcal{V}}_i)] = \mathcal{M}_i \dot{\omega}_i, \tag{1}$$

$$\partial_t(\rho \mathbf{u}) + \nabla \cdot (\rho \mathbf{u} \otimes \mathbf{u} + p\mathbb{I}) = \nabla \cdot \boldsymbol{\tau}, \tag{2}$$

$$\partial_t \rho \mathcal{E} + \nabla \cdot (\rho H \mathbf{u}) + \nabla \cdot \sum_i \rho_s \boldsymbol{\mathcal{V}}_i h_i = \boldsymbol{\tau} : \nabla \mathbf{u} - \nabla \cdot \mathbf{q} + \mathbf{J} \cdot E - \nabla \cdot \mathbf{q}_{\text{rad}}, \tag{3}$$

$$\partial_t \rho e_{\text{ev}} + \nabla \cdot (\rho e_{\text{ev}} \mathbf{u}) + \nabla \cdot \sum_i \rho_i \boldsymbol{\mathcal{V}}_i e_{\text{ev},i} = -\nabla \cdot \mathbf{q}_{\text{ev}} + \Omega^{ET} + \Omega^{C} + \Omega^{VT} + \mathbf{J} \cdot E - \nabla \cdot \mathbf{q}_{\text{rad}}, \tag{4}$$

where symbol ∂_t is the operator $\partial/\partial t$. The mass density of species i reads ρ_i, and its molar mass, $\mathcal{M}_i$. The mixture mass density is given by the expression $\rho = \sum_{j \in \mathcal{S}} \rho_j$, the mixture internal energy, $e = \sum_{j \in \mathcal{S}} \chi_j e_j$, with the mass fraction $\chi_i = \rho_i/\rho$, the mixture enthalpy $H = e + p/\rho$, the pressure $p = \rho RT \sum_{j \in \mathcal{H}} (\chi_j/\mathcal{M}_j) + \rho R T_{\text{ev}} \chi_e/\mathcal{M}_e$. The species internal energy e_i, $i \in \mathcal{S}$, comprises the translational contribution $[e_e = e_e^T(T_{\text{ev}})]$ for electrons; the translational, electronic, and formation contributions $[e_i = e_i^T(T) + e_i^E(T_{\text{ev}}) + e_i^F]$ for the atoms; and the translational, rotational, vibrational, electronic, and formation contributions $[e_i = e_i^T(T) + e_i^R(T) + e_i^V(T_{\text{ev}}) + e_i^E(T_{\text{ev}}) + e_i^F]$ for all the molecules. The specific total energy $\mathcal{E}$ is given by $\mathcal{E} = e + \frac{1}{2}\mathbf{u} \cdot \mathbf{u}$. The number of electronic levels used to compute the energy of the ions and molecules is tuned to yield the best matching agreement between values of the computed energies and the reference tables of Gurvich *et al* [43] are used. The rotational and vibrational energies of molecules are computed assuming the rigid rotor and harmonic oscillator approximations respectively. Spectroscopic constants used for defining thermodynamic properties pertaining to different internal energy modes are taken from [43]. Electronic specific data have been used for the vibrational and rotational constants of the molecules.

Changes in the chemical composition of the gas are modeled using source terms in the species conservation equations (1). The net chemical production rates are obtained

by summing the contribution of the individual chemical reactions as $\dot{\omega}_i = \sum_{r\in\mathcal{R}}(\nu_{ir}^b - \nu_{ir}^f)\tau_r$, where $\mathcal{R}$ indicates the set of chemical reactions, and the symbols ν_{ir}^f and ν_{ir}^b represent the forward and the backward stoichiometric coefficients of them ith species in reaction r. The contribution of a given reaction r to the species production source term, τ_r, can be expressed as:

$$\tau_r = k_r^f(T, T_{\rm ev})\prod_{j\in\mathcal{S}}\left(\frac{\rho_j}{\mathcal{M}_j}\right)^{\nu_{jr}^b} - k_r^b(T, T_{\rm ev})\prod_{j\in\mathcal{S}}\left(\frac{\rho_j}{\mathcal{M}_j}\right)^{\nu_{jr}^f} \qquad r\in\mathcal{R}. \tag{5}$$

The forward rate constant $k_r^f(T, T_{\rm ev})$ and backward rate constant $k_r^b(T, T_{\rm ev})$ are functions of both T and $T_{\rm ev}$ [44], and obey the relation $\mathcal{K}_r^{\rm eq} = k_r^f/k_r^b$, where the equilibrium rate constant is defined as:

$$\ln\mathcal{K}_r^{\rm eq}(T) = -\sum_{i\in\mathcal{S}}\left[(\nu_{ir}^b - \nu_{ir}^f)\frac{m_i g_i}{k_B T}\right], \tag{6}$$

where $g_i = h_i - Ts_i$ is the Gibbs free energy per molecule of species i. The influence of chemical reactions on the total and vibronic energy pools is modeled using Landau–Teller type relaxation form for Ω^{VT}, Ω^{ET} and by means of a non-preferential thermochemistry coupling for Ω_C. The rate of vibration-translation energy transfer is described as follows:

$$\Omega^{VT} = \sum_{m\in V}\rho_m\frac{e_m^V(T) - e_m^V(T_{vm})}{\tau_m^{VT}(T)}. \tag{7}$$

The average relaxation time is given by $\tau_m^{VT} = \sum_{j\in\rm H}(\rho_j/M_j)/\sum_{j\in\rm H}[\rho_j/(M_j\tau_{mj}^{VT})]$, where the inter-species relaxation time τ_{mj}^{VT} is based on Millikan–White's formula including Park's correction [45]. The energy lost by electrons through elastic collisions with heavy particles is written as:

$$\Omega^{ET} = \frac{\frac{3}{2}n_e k_B(T - T_{\rm ev})}{\tau_e^{ET}(T_{\rm ev})}. \tag{8}$$

The relaxation time is obtained from kinetic theory, $1/\tau_e^{ET} = \sum_{j\neq e}(m_e/m_j)\nu_{ej}$, where the collision frequencies read $\nu_{ej} = (8/3)v_e n_j\bar{\Omega}_{ej}^{11}$. Additional details on $\bar{\Omega}_{ej}^{11}$ and other collision integrals used for property calculations in the present work can be found in [46]. The expression of the chemistry vibronic energy coupling reads:

$$\Omega^C = \sum_{r\in\mathcal{R}}\alpha_r\dot{\omega}_r U^r, \tag{9}$$

where U^r is the reaction enthalpy of the r reaction, and $\dot{\omega}_r$, the chemical production term of the r reaction. The coefficient $\alpha_r \in [0, 1]$ is a calibration parameter discussed in [25]. The dominant contributions to this source term are: dissociation and ionization reactions. A common value of $\alpha_R = 1$ has been used for both ionization and dissociation reactions. For the remaining processes, α_R is set to 0.

The closure of the system of equations (1)–(4) requires the definition of transport properties to account for the diffusion of mass, momentum, and energy. The method developed by Chapman and Enskog gives expressions of the fluxes in terms of concentration, pressure and temperature gradients [27]. Viscous stress tensor as computed by the Chapman Enskog approximation reads:

$$\boldsymbol{\tau} = \mu(\boldsymbol{\nabla}\mathbf{u} + \boldsymbol{\nabla}^T\mathbf{u}) + \left(\kappa - \frac{2}{3}\mu\right)(\boldsymbol{\nabla}\cdot\mathbf{u})\mathbb{I}, \tag{10}$$

where μ is the shear viscosity and κ is the contribution due to the bulk viscosity, which is neglected in the present work. The convective heat-flux can be expressed as follow

$$\begin{aligned}\mathbf{q} &= -(\lambda^T + \lambda^R)\boldsymbol{\nabla}T - (\lambda^V + \lambda^E + \lambda^e)\boldsymbol{\nabla}T_{\rm ev},\\ \mathbf{q}_{\rm ev} &= -(\lambda^V + \lambda^E + \lambda^e)\boldsymbol{\nabla}T_{\rm ev},\end{aligned} \tag{11}$$

where λ^T and λ^R are the heavy particles translational and rotational thermal conductivities; λ^V, λ^E, and λ^e are the vibrational, electronic, and free electron translational thermal conductivities respectively. In this work, approximated expressions of the transport coefficients commonly referred to as mixture rules, have been adopted. Viscosity and heavy particle thermal conductivity are computed using Yos method, discussed by Gupta *et al* in [47]. The internal (e.g., rotational, vibrational and electronic) thermal conductivities are modeled using Euken's approximation [47]. The electron thermal and electrical conductivity are computed with the formulas developed by Devoto [48], where two non-vanishing Sonine polynomial contributions were found to yield accurate results [27]. The diffusion velocities $\boldsymbol{\mathcal{V}}_i$ obey Fick's law:

$$\rho_i\boldsymbol{\mathcal{V}}_i = -\rho_i D_i\boldsymbol{\nabla}\chi_i, \tag{12}$$

where $\chi_i = \rho_i/\rho$ indicates the mass fraction of the species i, and D_i is the mixture averaged diffusion coefficient. A more detailed description for individual transport properties can be found in [49]. Similar property models and system of governing equations have been used in the past to simulate flows in inductively coupled plasma generators [50–53].

2.2. Turbulence modeling

The computational cost incurred in resolving all the scales of turbulence for high enthalpy flows in arc-jets is prohibitive due to the size of the system of governing equations (1)–(3) and the complex property models being employed. Consequently, the flow equations are density-weighted time-averaged to produce the Favre-averaged Navier–Stokes (FANS) equations. A turbulence model is required when averaging over the nonlinear terms to close the system. The concept of eddy viscosity is introduced to model the effect of turbulence. The system of flow equations remains unaltered, but the variables now represent mean quantities and transport properties are modified to include eddy variables in the following manner: (a) $\mu \to \mu + \mu_t$, (b) $D \to D + D_t$, (c) $k \to k + k_t$, (d) and $\lambda \to \lambda + \lambda_t$. The eddy mass diffusivity D_t and thermal conductivity λ_t can be obtained from the eddy viscosity, μ_t:

$$D_t = \frac{\mu_t}{\rho\, Sc_t}, \tag{13}$$

$$\lambda_t = \frac{\mu_t\, C_p}{Pr_t}, \tag{14}$$

where Sc_t, Pr_t, and η are model parameters. The eddy viscosity is calculated using the Spalart–Allmaras (SA) one-equation model [54]. This requires an additional transport equation for the working variable $\nu_{\rm SA}$:

$$\frac{\partial \rho \nu_{\rm SA}}{\partial t} + \nabla \cdot (\rho \, \mathbf{u} \, \nu_{\rm SA}) = c_{b1} \, S_{\rm SA} \, \rho \, \nu_{\rm SA} - c_{w1} f_w \, \rho \left(\frac{\nu_{\rm SA}}{d}\right)^2 + \frac{1}{Pr_t} \cdot [(\mu + \rho \nu_{\rm SA} \, \nabla \nu_{\rm SA}] + \frac{c_{b2}}{Pr_t} \, \rho \, \nabla \nu_{\rm SA} \cdot \nabla \nu_{\rm SA}. \tag{15}$$

A set of algebraic closure relationships are solved to compute μ_t from $\nu_{\rm SA}$:

$$\mu_t = \rho \, \nu_{\rm SA} \, f_{v1}, \tag{16}$$

$$f_{v1} = \frac{\chi^3}{\chi^3 + c_{v1}^3}, \tag{17}$$

$$f_{v2} = 1 - \frac{\chi}{1 + \chi \, f_{v1}}, \tag{18}$$

$$\chi = \frac{\nu_{\rm SA}}{\nu}, \tag{19}$$

$$f_w = g \left(\frac{1 + c_{w3}^6}{g^6 + c_{w3}^6}\right)^{1/6}, \tag{20}$$

$$g = r + c_{w2}(r^6 - r), \tag{21}$$

$$r = \frac{\nu_{\rm SA}}{S_{\rm SA} \, \kappa^2 \, d^2}. \tag{22}$$

The present work uses a slightly modified form of the final closure function $S_{\rm SA}$, in order to ensure positivity.

$$S_{\rm SA} = \Omega + S_m, \tag{23}$$

where Ω is the vorticity magnitude and S_m is defined as follows:

$$S_m = \begin{cases} S_{m0}, & \text{if } S_{m0} \geqslant -c_{v2}\Omega, \\ \dfrac{\Omega(c_{v2}^2 + c_{v3} \, S_{m0})}{((c_{v3} - 2c_{v2})\Omega - S_{m0})}, & \text{otherwise.} \end{cases} \tag{24}$$

$$S_{m0} = \frac{\nu_{\rm SA}}{\kappa^2 \, d^2} f_{v2}. \tag{25}$$

2.3. Electric field equation

Without loss of generality, the electric field is split into an induced electric field $\mathbf{E}_{\rm i}$ and a gauge field ϕ so that,

$$\mathbf{E} = \mathbf{E}_{\rm i} - \nabla \phi. \tag{26}$$

Using Gauss' law, we have,

$$\nabla \cdot [\mathbf{J}] = \nabla \cdot [\sigma_e \, \mathbf{E}] = \nabla \cdot [\sigma_e \, \mathbf{E}_i] - \nabla \cdot [\sigma_e (\nabla \phi \,)] = 0, \tag{27}$$

where σ_e is the electric conductivity of the plasma. In arc-jets, the large constant current imposed at the anode is the main heating source of the plasma. We define the gauge field, ϕ, so that it satisfies:

$$\nabla \cdot [\sigma_e (\nabla \phi \,)] = 0 \tag{28}$$

along with the following boundary conditions:

$$-\sigma_e \nabla \phi = \mathbf{J}_c \text{ imposed current density at the anode surface,} \tag{29a}$$

$$\phi = 0 \text{ cathode is grounded,} \tag{29b}$$

$$\mathbf{n} \cdot \nabla \phi = 0 \text{ no current through the segmented walls.} \tag{29c}$$

The walls of the arc-jet consist of floating water-cooled copper electrically-floating segmented rings, resulting in a boundary condition described by equation (29*c*). The conductivity of the cells that contain an electrode face is artificially increased to $\sigma_e = 8 \times 10^3 \, \mathrm{S \, m^{-1}}$ [15]. This 'wall model' mimics the behavior of the thin sheath region near the electrode surface and ensures current continuity by enabling arc-attachment.

As mentioned above, the imposed current is expected to dominate the dynamics of the flow. Therefore, as a first approximation, $\mathbf{E}_i$ is set to 0. Once ϕ is obtained from the solution to equation (28), the Joule heating rate $\dot{\mathcal{S}}_{\rm joule}$ can be computed using:

$$\dot{\mathcal{S}}_{\rm joule} = (\sigma_e \nabla \phi) \cdot \nabla \phi. \tag{30}$$

2.4. Radiative transport equation

At high currents of the order of 10^3 A, the plasma in an arc-jet reaches temperatures close to 10^4 K. At the same time the walls of the facility have to be maintained at temperatures around 500 K. Under these conditions, radiative transfer within the plasma and to the walls starts to play a major role in the dynamics of the flow. Since radiative transport has a much smaller time scale compared to the plasma flow, radiative heat transfer is assumed to instantaneously adjust to any changes in flowfield conditions. For a non-scattering plasma, the steady state radiative transfer equation in the direction $\mathbf{\Omega}$ is expressed as:

$$\mathbf{\Omega} \cdot \nabla I_\nu = \eta_\nu - \kappa_\nu I_\nu = \kappa_\nu (\mathcal{S}_\nu - I_\nu), \tag{31}$$

where I_ν is the monochromatic light intensity per unit area. The opacity corresponding to a given frequency ν is denoted by κ_ν. Given the high-pressure in the arc-jet, the plasma is near equilibrium and opacities κ_ν can be computed assuming equilibrium air. Additionally, this allows Kirchhoff's law to be used for setting the emitted radiative flux, $\eta_\nu = \kappa_\nu \mathcal{S}_\nu$, where $\mathcal{S}_\nu$ is the black-body source function at ν.

The RTE is a first order differential equation and requires one boundary condition. The walls are assumed to radiate like black bodies into the domain:

$$I_\nu = B_\nu(T_w) \quad \text{if} \quad \mathbf{\Omega} \cdot \mathbf{n}_w > 0, \tag{32}$$

where $\mathbf{n}_w$ is the unit vector normal to the wall (pointing into the domain) and B_ν is the Plank's function. Even under the equilibrium assumption, a high number of frequencies, $O(10^6)$, are needed to resolve the opacity and emissivity for air. This makes calculating the radiative energy source computationally intensive and coupling the full radiative transfer to a fluid code impractical. There are several methods

available to reduce the computational requirements that involve strategies in averaging the equation before spatial integration. The present work uses the band averaging approximation. Multiplying equation (31) by $\mathrm{d}\nu$ and integrating over a frequency range, $b = [\nu_b, \nu_{b+1}]$, we get:

$$\boldsymbol{\Omega} \cdot \boldsymbol{\nabla} \bar{I}_b = \overline{\kappa_\nu B_\nu}|_b \; - \; \overline{\kappa_\nu I_\nu}|_b, \tag{33}$$

where,

$$\overline{f_b} = \int_{\nu_b}^{\nu_{b+1}} f_\nu \, \mathrm{d}\nu. \tag{34}$$

This leads to a closure problem since $\overline{\kappa_\nu I_\nu}|_b$ needs to be expressed in terms of averaged quantity, $\bar{I}_b$. The simplest model for remedying this assumes:

$$\overline{\kappa_\nu I_\nu}|_b = \tilde{\kappa}_b \bar{I}_b, \tag{35}$$

where the average opacity, $\tilde{\kappa}_l$, is defined as a Planck's function weighted average,

$$\tilde{\kappa}_b = \frac{\overline{k_\nu B_\nu}|_b}{\bar{B}_b}. \tag{36}$$

This closure works well when the spectral intensity I_ν is close to black body emission. The net heat flux for band b at a given point in space can be computed by integrating over the entire solid angle,

$$\mathbf{q}_b^{\mathrm{rad}} = \int_{4\pi} \bar{I}_b \, \boldsymbol{\Omega} \, \mathrm{d}\boldsymbol{\Omega}. \tag{37}$$

Finally, the total radiative heat flux is given by integrating the contributions from all frequencies:

$$\mathbf{q}^{\mathrm{rad}} = \sum_b \mathbf{q}_b^{\mathrm{rad}}. \tag{38}$$

3. Numerical method

The current simulation framework has been built around FIN-S hypersonic flow solver. This section reviews the numerical method used in FIN-S, followed by a description of the numerical formulations used to solve the electric and radiation fields. The process of loosely coupling the process of energy transfer due to Joule heating and radiation to the flowfield has also been discussed in this section.

The system of conservation equations (1)–(4), along with the transport equation for ν_{SA} (15), can be written in vector form as follows [55]:

$$\frac{\partial \mathbf{U}}{\partial t} + \frac{\partial \mathbf{F}_i}{\partial x_i} = \frac{\partial \mathbf{G}_i}{\partial x_i} + \dot{\mathcal{S}} \tag{39}$$

where $\mathbf{U} = [\, \rho_s, \rho u_j, \rho \mathcal{E}, \rho e_{\mathrm{ev}}, \rho \nu_{\mathrm{SA}} \,]^T$ is the vector of conservative variables, namely the species density, the cartesian components of mixture momentum per unit volume, the total mixture energy per unit volume, the mixture-averaged energy per unit volume corresponding to vibrational and electronic modes and the translational energy of free electrons, and the SA working variable. $\mathbf{F}_i$ and $\mathbf{G}_i$ represent the inviscid and viscous fluxes, respectively, in the ith direction. Equation (39) can be further simplified by splitting the inviscid flux vector into convective and pressure contributions and re-writing its divergence in terms of the inviscid flux Jacobian, $\mathbf{A}_i = \partial \mathbf{F}_i \,/\, \partial \mathbf{U}$:

$$\frac{\partial \mathbf{F}_i}{\partial x_i} = \frac{\partial \mathbf{F}_i^C}{\partial x_i} + \frac{\partial \mathbf{F}_i^P}{\partial x_i} = \mathbf{A}_i^C \frac{\partial \mathbf{U}}{\partial x_i} + \mathbf{A}_i^P \frac{\partial \mathbf{U}}{\partial x_i}. \tag{40}$$

This unconventional formulation for the inviscid flux is useful for implementing boundary conditions. Similarly, the divergence of the viscous flux vector $\mathbf{G}_i$ can be recast using the diffusivity matrix, $\mathbf{K}_{ij}$:

$$\frac{\partial \mathbf{G}_i}{\partial x_i} = \frac{\partial}{\partial x_i}\left(\mathbf{K}_{ij} \frac{\partial \mathbf{U}}{\partial x_j} \right). \tag{41}$$

Thus, the final strong form of the second-order system of governing equations is as follows:

$$\frac{\partial \mathbf{U}}{\partial t} + (\mathbf{A}_i^C \; + \mathbf{A}_i^P) \frac{\partial \mathbf{U}}{\partial x_i} = \frac{\partial}{\partial x_i}\left(\mathbf{K}_{ij} \frac{\partial \mathbf{U}}{\partial x_j} \right) + \dot{\boldsymbol{\mathcal{S}}}. \tag{42}$$

3.1. Stabilized finite element formulation

An upwind-biased test function is introduced to formulate the weak form for the system given by equation (42), [56],

$$\hat{\mathbf{W}} = \mathbf{W} \; + \; \tau_{\mathrm{SUPG}} \, \mathbf{A}_i \frac{\partial \mathbf{W}}{\partial x_i}, \tag{43}$$

where $\mathbf{W}$ is the original unbiased test function, $\mathbf{A}_i$ is the inviscid flux Jacobian, and τ_{SUPG} is a matrix that introduces the minimum amount of diffusion required to stabilize the scheme through upwind differencing. Multiplying equation (42) by the test function, equation (43), integrating by parts over the entire domain V, and adding a regularization term yields the SUPG weak statement: find $\mathbf{U}$ that satisfies the essential boundary and initial conditions for all $\mathbf{W}$ in an appropriate function space.

$$\begin{aligned} &\int_V \left[\mathbf{W} \cdot \left(\frac{\partial \mathbf{U}}{\partial t} \; + \; \mathbf{A}_i^P \frac{\partial \mathbf{U}}{\partial x_i} \; - \; \dot{\mathcal{S}} \right) \right. \\ &\quad \left. + \frac{\partial \mathbf{W}}{\partial x_i} \cdot \left(\mathbf{K}_{ij} \frac{\partial \mathbf{U}}{\partial x_j} - \mathbf{A}_i^C \frac{\partial \mathbf{U}}{\partial x_i} \right) \right] \mathrm{d}V \\ &\quad + \int_V \tau_{\mathrm{SUPG}} \frac{\partial \mathbf{W}}{\partial x_k} \cdot \mathbf{A}_k \left[\frac{\partial \mathbf{U}}{\partial t} \; + \; \mathbf{A}_i \frac{\partial \mathbf{U}}{\partial x_i} \right. \\ &\quad \left. - \frac{\partial}{\partial x_i}\left(\mathbf{K}_{ij} \frac{\partial \mathbf{U}}{\partial x_j} \right) - \; \dot{\mathcal{S}} \right] \mathrm{d}V \\ &\quad - \int_\Gamma \mathbf{W} \cdot (\mathbf{g} - \mathbf{f}) \mathrm{d}\Gamma = 0. \end{aligned} \tag{44}$$

The last term contains the normal components of the viscous fluxes, $\mathbf{g} = \mathbf{G} \cdot \hat{\mathbf{n}}$, and the convective inviscid fluxes, $\mathbf{f} = \mathbf{F}^C \cdot \hat{\mathbf{n}}$, on boundary Γ with unit normal $\hat{\mathbf{n}}$.

The stabilization matrix, τ_{SUPG}, is based on the work of Erwin *et al* [57] and includes the contributions of both inviscid and viscous terms.

$$\tau_{\mathrm{SUPG}}^{-1} = \sum_{i=\mathrm{nodes}} \left(\left| \frac{\partial \phi_i}{\partial x_j} \mathbf{A}_j \right| \; + \; \frac{\partial \phi_i}{\partial x_j} \mathbf{K}_{jk} \frac{\partial \phi_i}{\partial x_k} \right), \tag{45}$$

where ϕ_i is the shape function corresponding to the ith node in the finite element. The routine for computing the SUPG stabilization matrix at each quadrature point starts by assembling $\boldsymbol{\tau}_{\mathrm{SUPG}}^{-1}$, as outlined in equation (45). FIN-S employs the Eigen library [58] to then invert the relatively small matrix $\boldsymbol{\tau}_{\mathrm{SUPG}}^{-1}$ efficiently and obtain the final form for $\boldsymbol{\tau}_{\mathrm{SUPG}}$ that is used in equation (42). This procedure is evidently more expensive than some other approaches, but ensures that the stabilization matrix is independent of any heuristic definition of a flow-aligned length scale, and can be effectively used for wider variety of applications, even on highly stretched meshes [57]. Additional details on the current implementation of the SUPG stabilization method can be found in [18, 59].

3.2. Flow boundary conditions

In the case of supersonic outflow, the flow state at the boundary is defined completely by the information propagating from inside the domain. A no-slip and no-penetrating boundary condition is imposed as a Dirichlet condition on viscous walls without mass-injection. The condition $T = T_{\mathrm{wall}}$ is ensured on isothermal walls by including an additional Dirichlet constraint obtained by linearizing the residual equation $\mathcal{R} = (T - T_{\mathrm{wall}})$ with respect to the conservative variables [56, 60]. The same constraint-based approach is used to set $T = T_{\mathrm{ev}}$ at the wall surface. The convecting wall boundary condition has been designed to reduce numerical stiffness of the flow problem (when compared to the an isothermal wall), while providing a realistic description for the heating phenomenon [61, 62]. The energy flux normal to the wall surface leaving the flow domain is modeled using the convective heat transfer coefficient, h_c, and the ambient target temperature, T^*:

$$q_{\mathrm{wall}} = h_c(T - T^*). \tag{46}$$

A constant mass flux is imposed for walls with mass injection. This allows the wall normal velocity and consequently, the momentum flux to be specified at the boundary surface.

3.3. Flow solution methodology

Upon introducing a finite element discretization and the corresponding test functions, $\mathbf{W}_h$, equation (42) results in a transient, tightly coupled nonlinear system whose solution are the approximate unknown time dependent nodal values, $\mathbf{U}_n$:

$$\begin{aligned}\sum_{e=1}^{n_{\mathrm{el}}}\int_{\Omega_e}\Bigg[&\mathbf{W}_h.\left(\frac{\partial \mathbf{U}_h}{\partial t} + \mathbf{A}_i^P\frac{\partial \mathbf{U}_h}{\partial x_i} - \dot{\boldsymbol{\mathcal{S}}}_h\right)\\ &+ \frac{\partial \mathbf{W}_h}{\partial x_i}.\left(\mathbf{K}_{ij}\frac{\partial \mathbf{U}_h}{\partial x_j} - \mathbf{A}_i^C\frac{\partial \mathbf{U}_h}{\partial x_i}\right)\Bigg]\mathrm{d}\Omega\\ &+ \sum_{e=1}^{n_{\mathrm{el}}}\int_{\Omega_e}\tau_{\mathrm{SUPG}}\frac{\partial \mathbf{W}_h}{\partial x_k}.\mathbf{A}_k\Bigg[\frac{\partial \mathbf{U}_h}{\partial t} + \mathbf{A}_i\frac{\partial \mathbf{U}_h}{\partial x_i}\\ &- \frac{\partial}{\partial x_i}\left(\mathbf{K}_{ij}\frac{\partial \mathbf{U}_h}{\partial x_j}\right) - \dot{\boldsymbol{\mathcal{S}}}_h\Bigg]\mathrm{d}\Omega = 0.\end{aligned} \tag{47}$$

$\mathbf{U}_h(\mathbf{x}, t)$ is re-constructed using the finite element basis functions, $\{\psi\}$ and the nodal solution values: $\mathbf{U}_h(\mathbf{x}, t) = \sum_j \psi_j(\mathbf{x})\mathbf{U}_h(\mathbf{x}_j, t)$. The current study uses a standard piecewise linear Lagrange basis for this interpolation, resulting in a second-order accurate scheme. Time-stepping is carried out by advancing the solution $\mathbf{U}_{n+1} \equiv \mathbf{U}_h(t_{n+1})$ at time t_n by a time step $\Delta t = t_{n+1} - t_n$. A backward Euler difference scheme is used to obtain first order accurate in time formulation which provides maximum stability. $\partial\,\mathbf{U}_{n+1}/\partial t$ is approximated as $(\mathbf{U}_{n+1} - \mathbf{U}_n)/\Delta t$. The time-discretized equations are written in residual form to form a nonlinear algebraic system:

$$\mathbf{R}(\mathbf{U}_{n+1}) = 0 \tag{48}$$

Equation (48) can be further reduced to a series of linear problems, which upon solving, converge to the solution, $\mathbf{U}_{n+1}$, of the nonlinear system. Taylor series expansion of (48) about iterate $\mathbf{U}_{n+1}^l$ results in the standard expression for Newton's method:

$$\left[\frac{\partial \mathbf{R}(\mathbf{U}_{n+1}^l)}{\partial \mathbf{U}_{n+1}}\right]\delta\mathbf{U}_{n+1}^{l+1} = -\mathbf{R}(\mathbf{U}_{n+1}^l), \tag{49}$$

where $\partial\mathbf{R}/\partial\mathbf{U}$ is the Jacobian for the nonlinear system and $\delta\mathbf{U}_{n+1}^{l+1} = \mathbf{U}_{n+1}^{l+1} - \mathbf{U}_{n+1}^l$. The implicit linear system for $\delta\mathbf{U}_{n+1}^{l+1}$ solved for a sequence of iterates ($l = 0, 1, \ldots$) converges to $\mathbf{U}_{n+1}$. The use of piece-wise linear elements results in a large system matrix which is sparse. FIN-S employs the parallel sparse matrix format made available through the PETSc toolkit, along with PETSc Krylov subspace iterative solvers [63]. A parallel block-Jacobi ILU(0) preconditioner is used for the present work [64, 65]. The METIS unstructured graph partitioning library [66] is used to achieve non-overlapping domain decomposition with a unique set of elements assigned to each processor.

3.4. Electric field

The electric field and flow-field calculations are loosely coupled at every time-step. The computed flow solution is used to obtain the distribution for electrical conductivity in the domain. This is then used for solving the electric field equation, equation (28), and upgrade the Joule heating term. The energy addition due to the electrical discharge is treated as an explicit source term and is held constant while advancing the system of flow equations to the next time step. A two-way coupling ensues—Joule heating modifies the conductivity of the operating gas, σ_e, which in turn results in an altered electrical field distribution. It is worth mentioning that no turbulent electrical conductivity is considered in the present paper. Thus, the present model should be extended to explicitly account for a turbulent contribution to the electrical conductivity consistent with the SA one-equation model [31].

The weak form for the electric field equation (28) is again obtained through the standard technique of multiplying the original equation by a set of test functions, $\mathbf{W}_{\mathrm{el}}$, and integrating over the entire domain, V. The equation is elliptic in nature and can be solved accurately using the standard Galerkin formulation without any additional stabilization. Thus, Ω satisfies the essential boundary conditions, given a distribution of electrical conductivity, σ_e, for all $\mathbf{W}_{\mathrm{el}}$ in an

appropriate function space.

$$\int_V \sigma_e \frac{\partial \mathbf{W}_{\text{el}}}{\partial x_i} \cdot \frac{\partial \phi}{\partial x_i} \, \mathrm{d}V - \int_\Gamma \mathbf{W}_{\text{el}} \, \epsilon \, \mathrm{d}\Gamma = 0, \tag{50}$$

where ϵ is the imposed current density normal to a boundary surface, Γ, with natural boundary conditions. Current continuity at the electrode with essential boundary condition is ensured by setting the electrical conductivity in the immediate vicinity of the electrode surface to a high value ($\sim 8 \times 10^3$ S m^{-1}) as described by Trelles *et al* [15]. This is critical for ensuring stable arc attachment despite the use of a common temperature for all internal energy modes. A piecewise linear Lagrange basis $\{\psi\}$ is again employed to express values of the electrical potential and the Joule heating term in terms of the nodal solution (ϕ_h):

$$\phi(\mathbf{x}) = \sum_j \psi_j(\mathbf{x}) \phi_j(\mathbf{x}_j), \tag{51}$$

$$\dot{\mathcal{S}}_{\text{joule}}(\mathbf{x}) = \left[\sum_i \psi_i(\mathbf{x}) \sigma_e(\mathbf{x}_i) \right] \left\| \sum_j \nabla \psi_j(\mathbf{x}) \phi_j(\mathbf{x}_j) \right\|^2 \tag{52}$$

The discretized electric field equation is solved using PETSc Krylov subspace linear iterative solvers in conjunction with the algebraic multigrid preconditioner [63].

3.5. Radiative heating

Since total radiative heat flux is computed by integrating the radiative intensity over the complete solid angle, equation (31) needs to be discretized in both the spatial and angular domains. The discrete-ordinates method is employed to obtain a set of 1D RTE equations in discrete directions, $\mathbf{\Omega}^m$. The integral over the solid angle is replaced by a weighted vector sum of radiative intensities in these discrete directions to obtain the net radiative flux at a given point:

$$\mathbf{q}^{\text{rad}} = \int_{4\pi} I_\lambda \, \mathbf{\Omega} \, \mathrm{d}\mathbf{\Omega} = \sum_m w^m \, I_\lambda^m \, \mathbf{\Omega}^m. \tag{53}$$

w^m and I_λ^m are the quadrature weight and radiative intensity associated with direction $\mathbf{\Omega}^m$. A Gaussian type quadrature is employed to determine $\mathbf{\Omega}^m$ and the corresponding weights [67, 68] for different degrees of approximation. The discrete-ordinate form of the RTE can be recast into the weak form through the traditional Galerkin approach using a set of test functions, $\mathbf{W}_r$, in an appropriate function space:

$$\int_V \mathbf{W}_r [\mathbf{\Omega}^m \cdot \nabla I_\lambda^m + \kappa_\lambda I_\lambda^m] \partial V = \int_V \mathbf{W}_r \, \kappa_\lambda \, \mathcal{S}_\lambda \, \partial V, \tag{54}$$

where I_λ^m is the radiative intensity in the m direction, corresponding to λ wavelength. The wall of the arc-heater is assumed to be radiating in the inward direction (towards the centerline) as a black body at the wall temperature. Therefore, $I_\lambda^m = \kappa_\lambda \, \mathcal{S}_\lambda(T_{\text{wall}})$ on the boundary surface Γ with an outward normal, $\hat{\mathbf{n}}$, if $\mathbf{\Omega}^m \cdot \hat{\mathbf{n}} < 0$. No constraints are placed on the radiative flux in the outward direction (away from the centerline). The convection dominated characteristics of RTE introduces spurious oscillations during the numerical modeling of the radiative transfer process using conventional unbiased test functions. Thus, $\mathbf{W}_r$ is augmented by introducing streamline diffusion in order to overcome the stability problem without introducing any additional consistency error:

$$\hat{\mathbf{W}}_r = \kappa_\lambda \, \mathbf{W}_r + \mathbf{\Omega}^m \cdot \nabla \, \mathbf{W}_r. \tag{55}$$

$\hat{\mathbf{W}}_r$ is a simplified form of the stabilized test function used by Liu [69] for simulating radiation in a graded index medium. This formulation is derived by applying the least-squares finite element method to the radiative transfer equation. The current choice of $\hat{\mathbf{W}}_r$ for stream wise biasing also eliminates dependence on a tunable free parameter, for defining the amount of additional stabilizing diffusion, found in other formulations [70, 71]. Thus, the radiation solution procedure does not need to be re-calibrated with changing flow conditions. A piecewise linear Lagrange basis $\{\psi\}$ is again employed as the set of unbiased test functions $\mathbf{W}_r$ and is used to interpolate the radiative intensity using nodal values. The block Jacobi preconditioner [63] is used while solving the discretized radiative transfer equations.

Computing the total radiative heat flux by iteratively summing the contribution of each spectral frequency in a line-by-line calculation is prohibitively expensive due to the highly non-gray spectral properties of high temperature air. The current study uses a multi-band reduction approach implemented by Scoggins *et al* [72] for high temperature air in LTE. The total frequency range encompassing the different radiative processes have been divided into contiguous sets of frequencies called bins. Individual radiative processes have been assigned to different bins based on the spectral wavelength. The averaged opacity and source functions for bins have been computed *a priori*, and used for generating look-up tables based on pressure and temperature. Spectral absorption coefficients for bound-bound, bound-free, and free-free radiative processes for LTE air in the wavelength range of 0.04–20 μm were tabulated using the non-equilibrium air radiation code (NEQAIR) [73] developed at NASA Ames Research Center. These have been classified into 100 bins to create a reduced spectral model capable of capturing the dominant absorption and emission phenomenon encountered during the present investigation. A more detailed description of the original line database for air and the subsequent binning strategy can be found in [72]. The divergence of the total radiative heat flux at any point inside an element can be reconstructed using the shape functions and the net nodal fluxes. Since, spatial dependence is limited only to the shape functions, radiative heating can easily be expressed as:

$$\nabla \cdot \mathbf{q}_{\text{rad}} = \sum_j \frac{\partial \phi_j}{\partial x} q_{\text{rad}}^x(\mathbf{x}_j) + \frac{\partial \phi_j}{\partial y} q_{\text{rad}}^y(\mathbf{x}_j) + \frac{\partial \phi_j}{\partial z} q_{\text{rad}}^z(\mathbf{x}_j). \tag{56}$$

The discrete-ordinate method combined with finite-element discretization allows the RTE to be solved using the same mesh decomposition strategy and parallel framework as the flow solver. The use of a common computational mesh further simplifies the process of efficiently coupling these disparate physical processes with the flow calculations.

4. Results

The new simulation framework is employed to simulate the dynamics of plasma discharge in the 20 MW constricted arc heater AHF at NASA Ames Research Center. An effort has been made to not only present flowfield solutions but also describe the simulation procedure employed for this challenging problem. This work focuses on showcasing the various capabilities of the loosely-coupled multi-physics approach through the phenomenological description of the flow inside the AHF. Although detailed parametric studies and comparison with experimental data will be completed in future, a series of tests have been performed to verify/validate individuals modules of the full framework:

(1) The base code for FIN-S has been extensively verified using the method of manufactured solutions for both laminar and turbulent flows [74, 75].
(2) The suitability of the SA one-equation model for simulating turbulent internal flows has been established by validating computational results using experimental data obtained by Mckeon *et al* for fully developed turbulent pipe flows at the Princeton/DARPA-ONR SuperPipe Facility [76].
(3) The electric field module based on the simplified Poisson's formulation has been verified using manufactured solutions.
(4) Radiative heating has been verified using semi-analytical solutions obtained for radiative transfer inside a sphere with prescribed temperature profiles [77].

4.1. Problem description and solution procedure

The computational grid for the AHF is presented in figure 1. It is a multi-block structured mesh and consists of approximately 410 000 elements. Some simplifications have been made to the AHF geometry while constructing this mesh. In particular, grooves on the electrode surface created by a series of alternating copper rings and spacer disks have been replaced by a continuous straight edge of equivalent length. The throat is located at the origin of the coordinate system. The test gas is introduced in the axial direction through the segmented disks along the length of the constrictor. This injection has an additional azimuthal (swirl) velocity component that enables enhanced mixing and stabilization the arc current. Consequently, the gas enters the facility at an angle of 45° to the radial direction. Additionally, a small quantity of 'shield gas' (assumed to be the same as the test gas for this study) is pushed into the anode chamber to shield the electrodes. The walls of the heater are water cooled to protect them from the strong heating due to electrical discharge. The exact location and size of the conducting surfaces for the two electrodes are highlighted in figure 2. The operating parameters for the AHF have been listed in table 1.

A convection type boundary condition (equation (46)), with $h_w = 10^6\ \mathrm{W\ m^{-2}\ K^{-1}}$, is imposed on the electrode surface and the walls of the constrictor, with the specified wall temperature acting as the target temperature. The use of this boundary condition lends a degree of control over how strictly the target temperature is imposed. The overall stability of the simulation has been improved by initially setting h_w to a low value (nearly adiabatic wall) and then gradually increasing it to its final value. This prevents simulation failures, despite high temperature gradients, and ensures that the correct wall temperature gets enforced. Numerical investigations indicate that flow-field solutions become largely invariant for $h_w > 10^5$, which corresponds to heat transfer for high-pressure flow in a pipe [61]. An isothermal no-slip wall condition is imposed on all other walls. A test gas mixture composed of 11-species air at equilibrium is injected through the surface of the anode and the walls of the constrictor. The arc-jet exit which is located just downstream of the throat is modeled as a supersonic outflow. A constant current density based on the total operating current is imposed on the anode surface. The cathode is grounded and the electric potential at its surface set to zero. In order to improve numerical stability, the total current supplied to the arc heater is ramped up linearly at every iteration until it reaches the stipulated operating value. The walls are assumed to be non radiating. This assumption is justified by the low value of the imposed wall temperature. In the computation of the radiative flux, the integration over the solid angle is approximated by a twenty four-point Gaussian quadrature. Time marching is carried out with time-steps varying between 10^{-7} and 10^{-6} s. This is done to mitigate the impact of a transient upsurge in instabilities when the electric current and the associated Joule heating is activated. The flow-field eventually stabilizes, with a distinct pathway comprising of hot gases, forming for the flow of the electric current. The flow becomes completely developed at that point with the only source of unsteadiness being the constantly shifting asymmetric arc attachment in the cathode chamber. The solution at $t = 4540.2$ μs after the total imposed current reaches its operating value outlined in table 1 is used analyze the different flow features. A comparison between solutions at times 572.6, 765.2 and 2140.2 μs is used to discuss the unsteady nature of the flowfield.

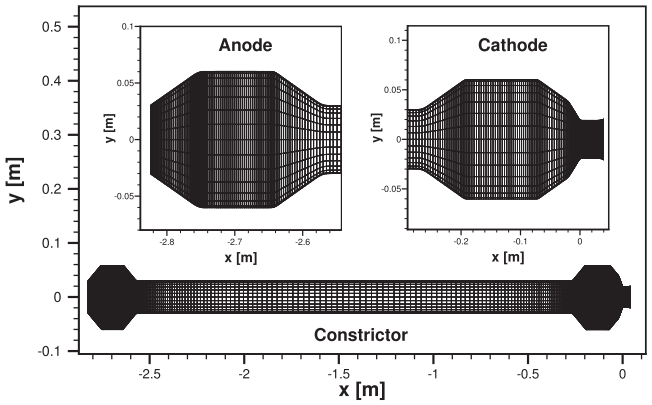

Figure 1. Computational grid for modeling the 20 MW Aerodynamic Heating Facility (AHF).

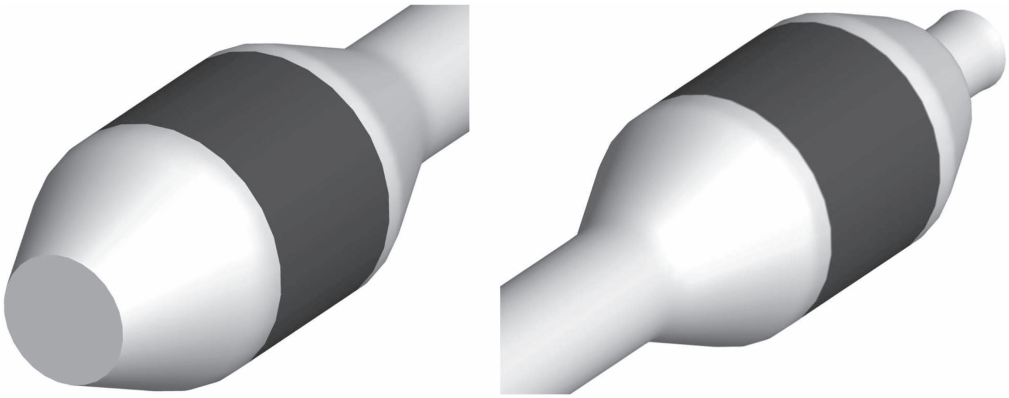

Figure 2. Location and size of the anode (left) and cathode (right). The conducting surfaces of each electrode are highlighted in black.

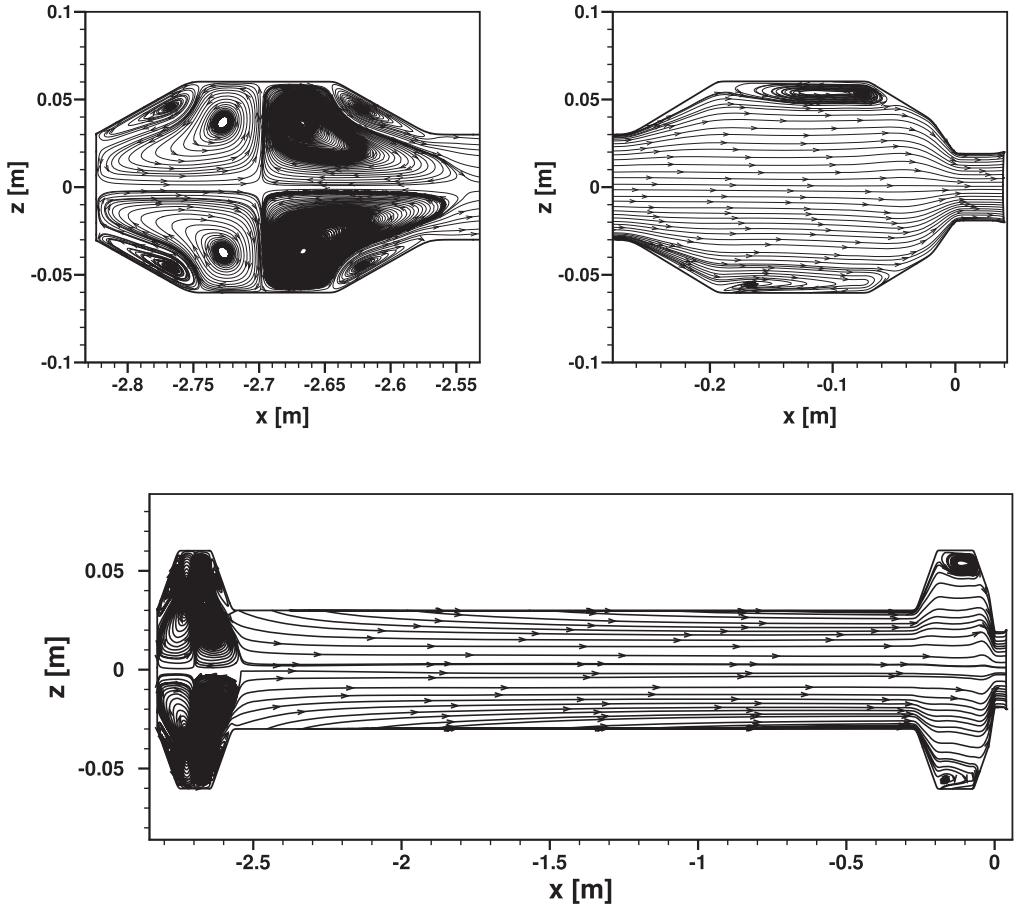

Figure 3. Flow streamlines in the anode chamber (top-left), the cathode chamber (top-right), and the constrictor (bottom) of the 20 MW Aerodynamic Heating Facility (AHF) along the vertical plane.

4.2. Simulation results

The physico-chemical characteristics of the AHF are outlined in this section through the distribution of various properties in the three-dimensional flow domain. The results are presented on different cross-sectional slices and along the center-line axis.

4.2.1. Flowfield in anode and constrictor. Figure 3 presents the flow streamlines in the three main regions of the AHF along the vertical plane. The process of axisymmetric mass injection is clearly highlighted in this figure with streamlines starting from the walls of the anode (shield gas) and the constrictor (test gas). The radially directed shield gas starts accelerating in the transverse direction as it approaches the axis. This results in the formation of a pair of large contrarotating vortex system in the anode chamber. The size and location of these vortices oscillate in time, introducing small asymmetric perturbations. However, these disturbances are damped out quickly as the flow moves downstream and

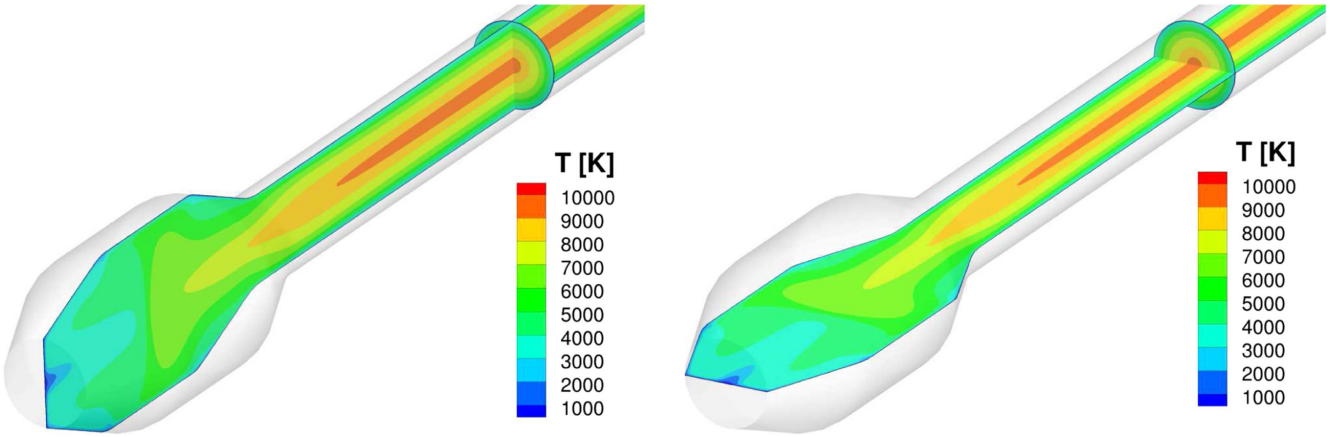

Figure 4. *Rotational-translational* temperature T distribution in the anode chamber: along the vertical plane (left) and the horizontal plane (left).

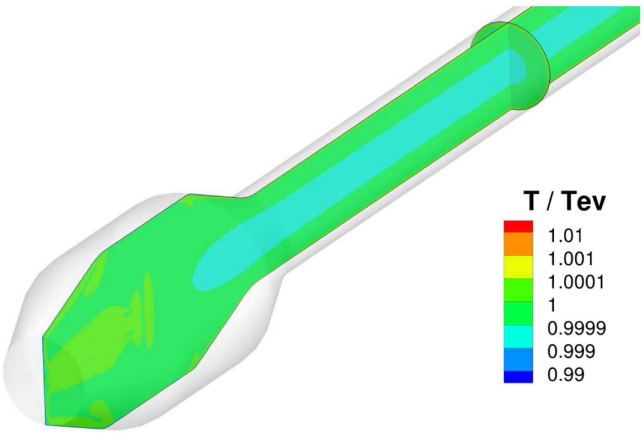

Figure 5. Ratio of *rotational-translational* temperature T to *electro-vibrational* temperature T_{ev} along the vertical plane in the anode chamber.

Table 1. AHF operating parameters.

Test, shield gas	Air-11
Wall temperature, K	500
Total current, A	1600
Constrictor mass injection rate, g s^{-1}	500
Anode mass injection rate, g s^{-1}	25

starts accelerating in the axial direction. This results in an axisymmetric flowfield in the anode chamber and the constrictor. This is a direct consequence of the absence of any asymmetry in the boundary conditions (uniform mass injection and current density) or geometry in these regions. Figures 4 and 5 highlight this symmetry by presenting the distribution of T and the ratio between T and T_{ev} along different planes in the anode chamber and the constrictor. Figure 5 clearly indicates that the higher pressures inside the facility quickly drives the gaseous mixture to LTE with $T = T_{ev}$.

The electric field interacts with the flow through the process of energy addition through Joule heating. A combination of cool gas being injected and heat loss away from the fluid domain results in lower temperatures near the walls. This opens up a high temperature channel along the centerline of the constrictor, with large temperature gradients in the radial direction. A self-sustaining coupling is established—higher temperatures results in larger electrical conductivity (due to greater degree of ionization and higher free electron density), increasing current density and the subsequent Joule heating (figure 6). Since, the basic flow through the anode chamber and constrictor is axisymmetric, the distribution of electrical conductivity is axisymmetric as well (figure 6). This coupled with a uniform current density being imposed on the anode results in an electric field that is axisymmetric in these regions as well. Thus, electric discharge and the resultant Joule heating only strengthens the underlying flow symmetry.

4.2.2. Unsteady asymmetric arc attachment in cathode chamber. The three-dimensional nature of the plasma flow inside the arc-heater is clearly evident from figure 7, which shows the T distribution in the cathode chamber. Similar plots for T_{ev} have not been presented since the flowfield continues to be in a state of thermal equilibrium in the cathode chamber. The formation of a constricted arc attachment in a unique direction at a given time instance has a strong impact on the flow-field, introducing asymmetry in the distribution of flow properties. The size and location of the arc attachment is shown in figure 8 through the distribution of current density and Joule heating along different cross-sections and at the cathode's surface. As the flow travels from the constrictor to the cathode, the cross-sectional area increases rapidly. This induces flow separation and the formation of recirculation regions (figure 3).

The vortex structures in this region originally have a small degree of asymmetry due to numerical errors, which result in an uneven distribution of flow properties. Even if the difference in electric conductivity is marginal, the current attempts to flow through regions with higher values of σ_e and starts becoming asymmetric. Since, the entire cathode is at the same electric potential and no breakdown or sheath model is

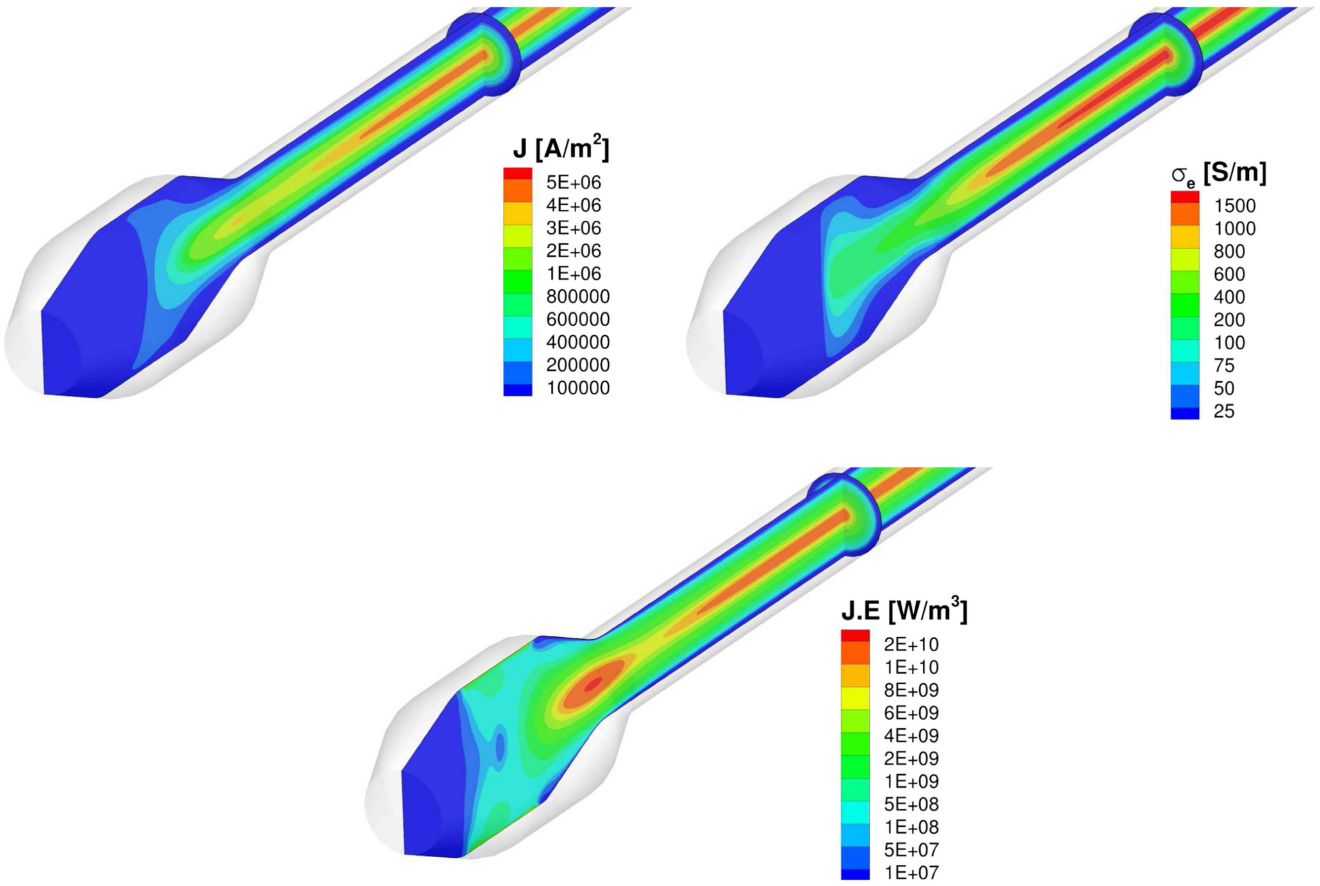

Figure 6. Electrical properties in the anode chamber: current density (top-left), electrical conductivity (top-right), and Joule heating (bottom).

employed, the arc attaches to the surface wherever it gets close enough to the cathode. As a direct consequence of the arc attachment, most of the current now travels through a narrow plasma column connected to a specific spot on the cathode surface. Electric conductivity is an increasing function of temperature, which initiates a self-sustaining process; higher current densities inside the plasma column result in more heating and consequently, larger values of electrical conductivity. Thus, the main source of asymmetry in the flow through the cathode region is the electric field. This behavior is not observed at the anode because a uniform current density (and not potential) is imposed at its surface. This ensures that Joule heating (which is driven by the current density) is not concentrated in a particular region and the flow continues to be axisymmetric. The required level of proximity for arc attachment to occur depends on the thickness of the region around the cathode where artificially high electrical conductivity is being imposed ($\sim$0.2 mm for the current study).

The current analysis uses the two-temperature thermal non-equilibrium model which considers the translational energy of free electrons to be in equilibrium with the vibrational and electronic energy of heavy particles. In light of T_{ev} reflecting the contributions of vibrational and electronic energies of heavy particles as well, an isothermal boundary condition is imposed instead of forcing a zero-gradient (adiabatic) [62]. This results in T_{ev} decreasing in the vicinity of the electrode wall and necessitating the use of an artificially high value of electrical conductivity for current continuity. Future work will focus on adding an additional temperature to characterize the energy of free-electrons. This modification coupled with improved sheath and breakdown models would eliminate the need for an arbitrary layer with inflated electrical conductivity and provide a more physical description of arc attachment and energy transfer at the electrodes.

The time-evolution of the current density is displayed in figures 9 and 10, clearly highlighting the dynamic behavior of the arc-attachment process. Trelles *et al* [78] have described different possible mechanisms that can induce this process of reattachment. The interplay between forces generated due to the interaction of the arc, consisting of hot plasma, with the surrounding gas flow and the local electric field causes the attachment point to constantly keep shifting. The arc-column appears to behave like a solid-body. The drag force exerted on it by the flowfield induces a net angular momentum. This results in the column twisting and forming a new attachment point. This unsteady behavior can also be viewed as the flowfield dragging the arc column further downstream, which increases the arc length and consequently, the voltage drop across it. This causes the arc to start seeking out a shorter path, resulting in the old connection being snapped and a new attachment point being established. Thus, a three-dimensional

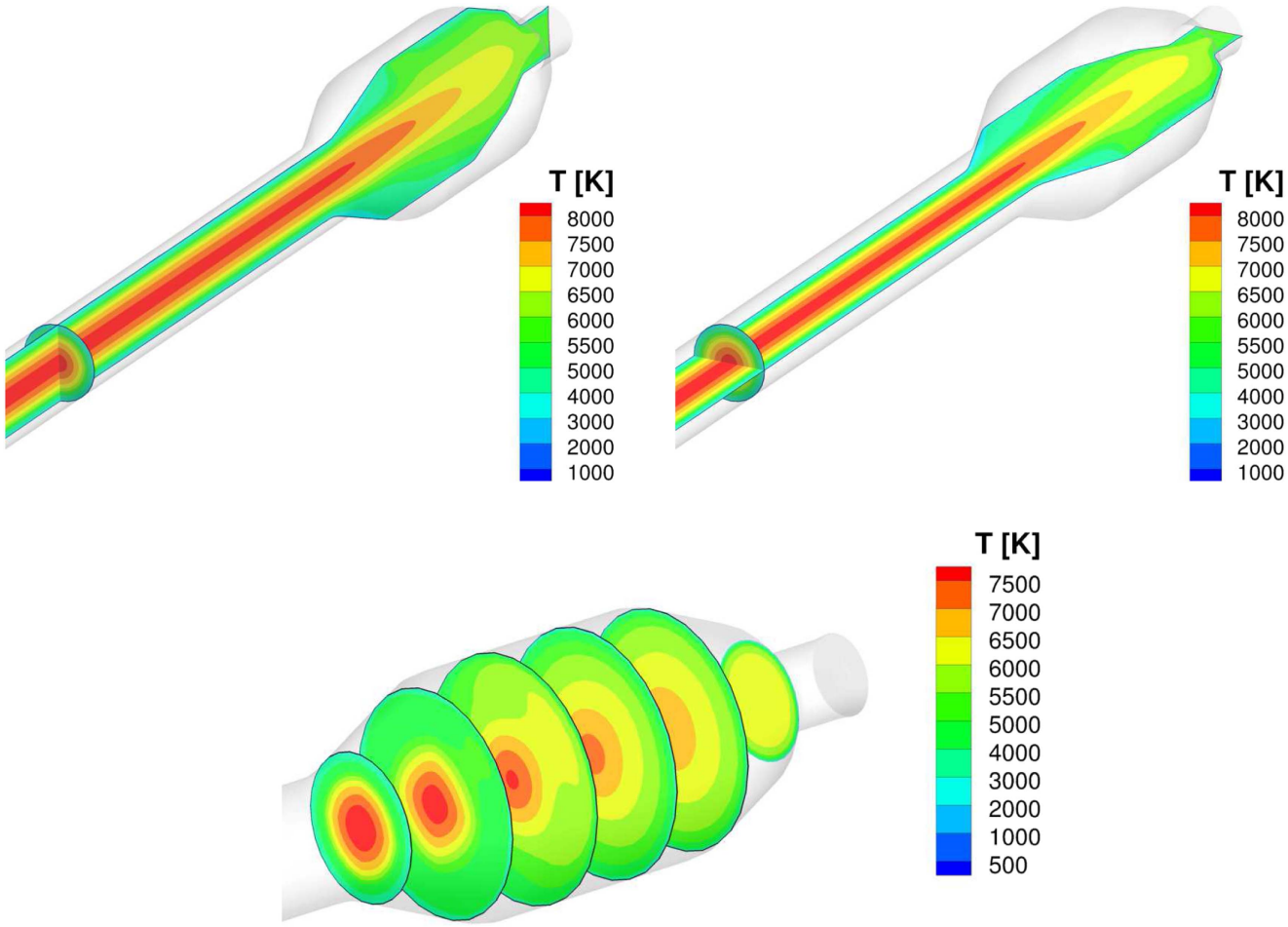

Figure 7. *Rotational-translational* temperature T distribution in the cathode chamber: along the vertical plane (top-left), the horizontal plane (top-right), and different axial cross-sections (bottom).

unsteady treatment of the governing equations is crucial for capturing the true dynamics of these facilities.

Although the present work precludes Lorentz forces generated due to the magnetic field, *a posteriori* analysis has been performed to assess their impact on the flowfield. The induced magnetic field $\mathbf{B}$ is obtained using the current density $\mathbf{J}$ from electrostatic calculations:

$$\nabla^2 A = \mu_o \mathbf{J}, \tag{57}$$

$$\mathbf{B} = \nabla \times \mathbf{A}. \tag{58}$$

Figure 11 presents the magnitude of the induced magnetic field in the different sections of the AHF. A β parameter for the plasma discharge [79] can be computed in the following manner:

$$\beta = \frac{\text{Hydrodynamic pressure}}{\text{Magnetic pressure}} = \frac{P}{(\mathbf{B}\cdot\mathbf{B})/(2\times\mu_o)}. \tag{59}$$

The distribution of β corresponding to the self-induced magnetic field is plotted in figure 12. A high value of β (10^2–10^5) indicates the possible impact of self-induced magnetic field in terms of its ability to initiate instabilities would be minimal, and hydrodynamic forces would dominate. This a direct consequence of the high pressures inside the facility and relatively low total imposed current. Nevertheless, it should be noted that a solution for both self-induced and external magnetic fields would allow the behavior of the electric arc to be resolved with greater accuracy. The resultant Lorentz forces are expected to impact the AHF flowfield in the following manner: (1) introduction of magnetic pinching [62] especially in the constrictor, which would decrease the cross-sectional area of the arc column, (2) increased kink instabilities [62] in regions where the arc column is curved, (3) and higher rate of rotation and subsequent asymmetric re-attachment of the arc column in the cathode chamber, primarily due to the external magnetic field [80]. Consequently, accounting for the self-induced and external magnetic fields in future studies would allow investigation of magnetic instabilites and enable more accurate modeling of the dynamics of the plasma column and the re-attachment process.

4.2.3. Impact of radiative heat transfer and turbulence.

Radiation plays a key role in re-distributing the energy being added to the flowfield through the electric discharge. The distribution of radiative heating in the arc-jet is presented in figure 13 for both the anode and cathode regions. As the

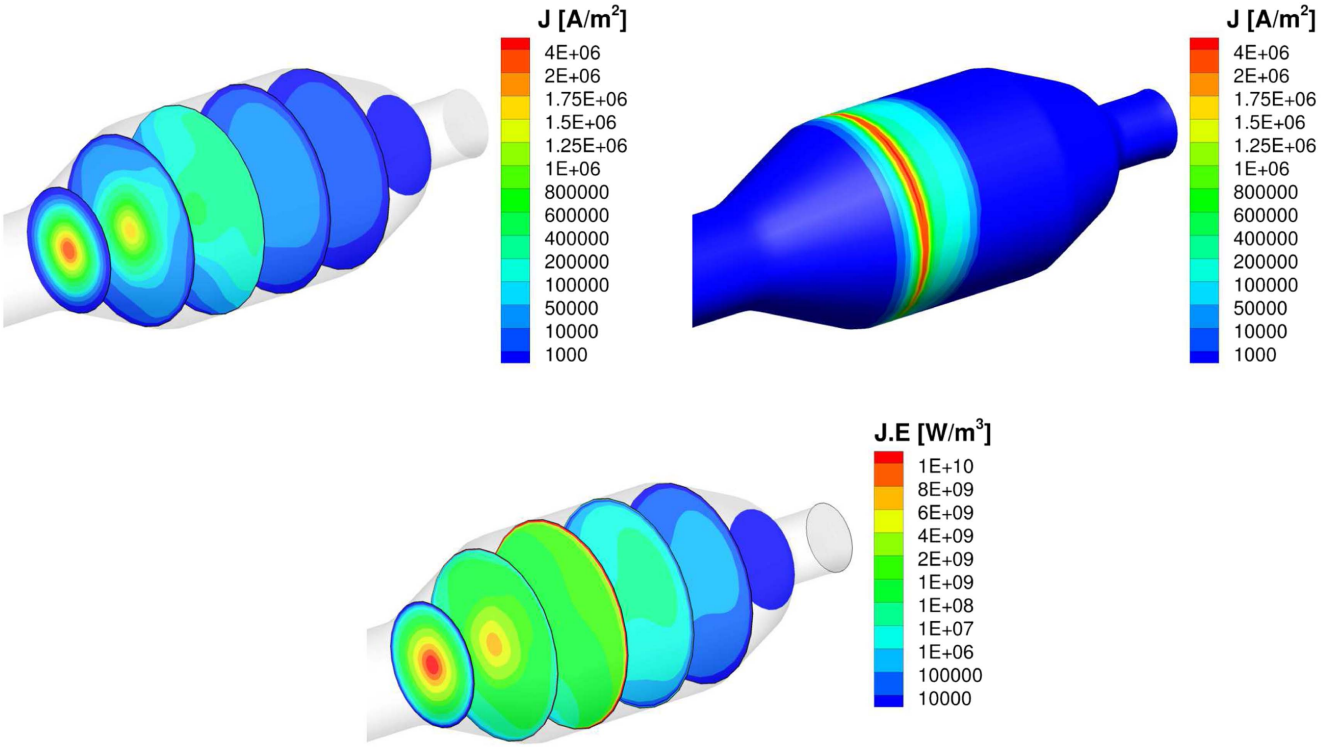

Figure 8. Electrical properties in the cathode chamber: current density along different axial cross-sections (top-left) and over the cathode surface (top-right), and Joule heating along different axial cross-sections (bottom).

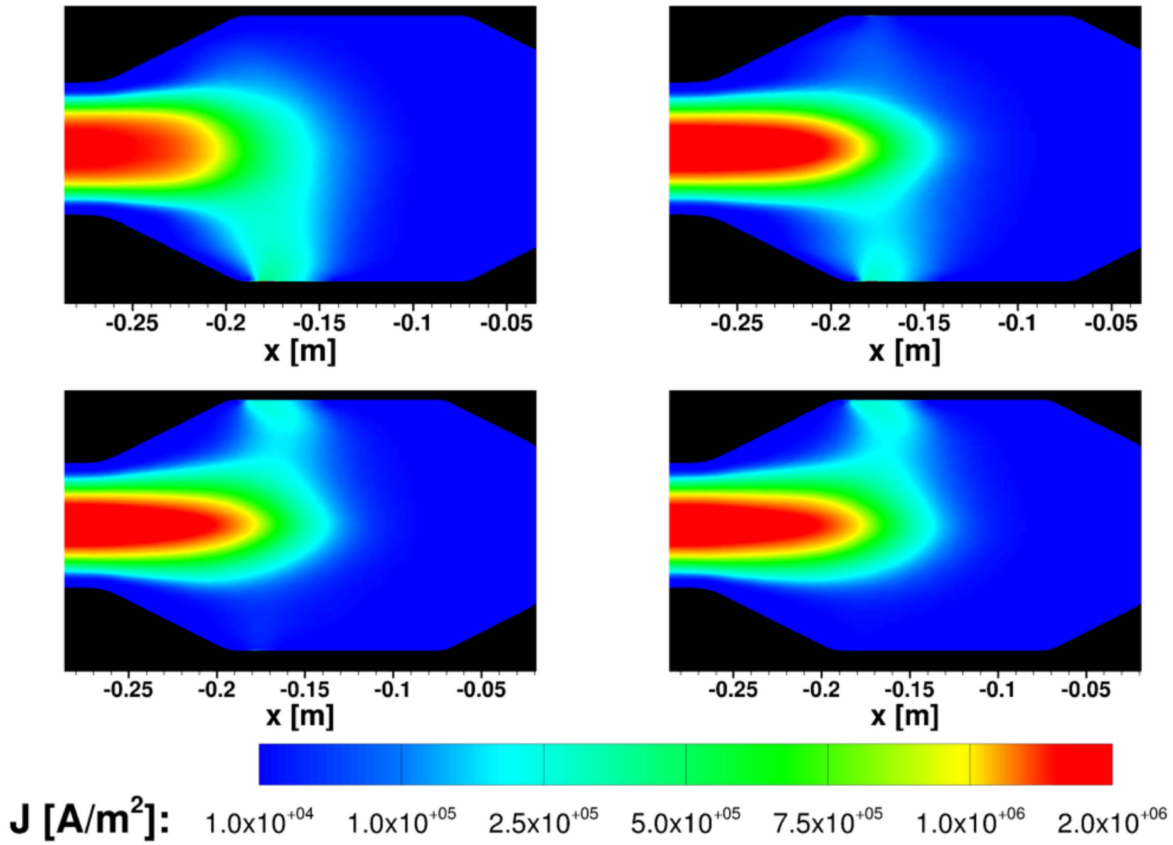

Figure 9. Formation of new attachment point: current density along the vertical plane at $t = 572.6\ \mu$s (top-left), $t = 765.2\ \mu$s (top-right), $t = 2140.2\ \mu$s (bottom-left), and $t = 4540.2\ \mu$s (bottom-right).

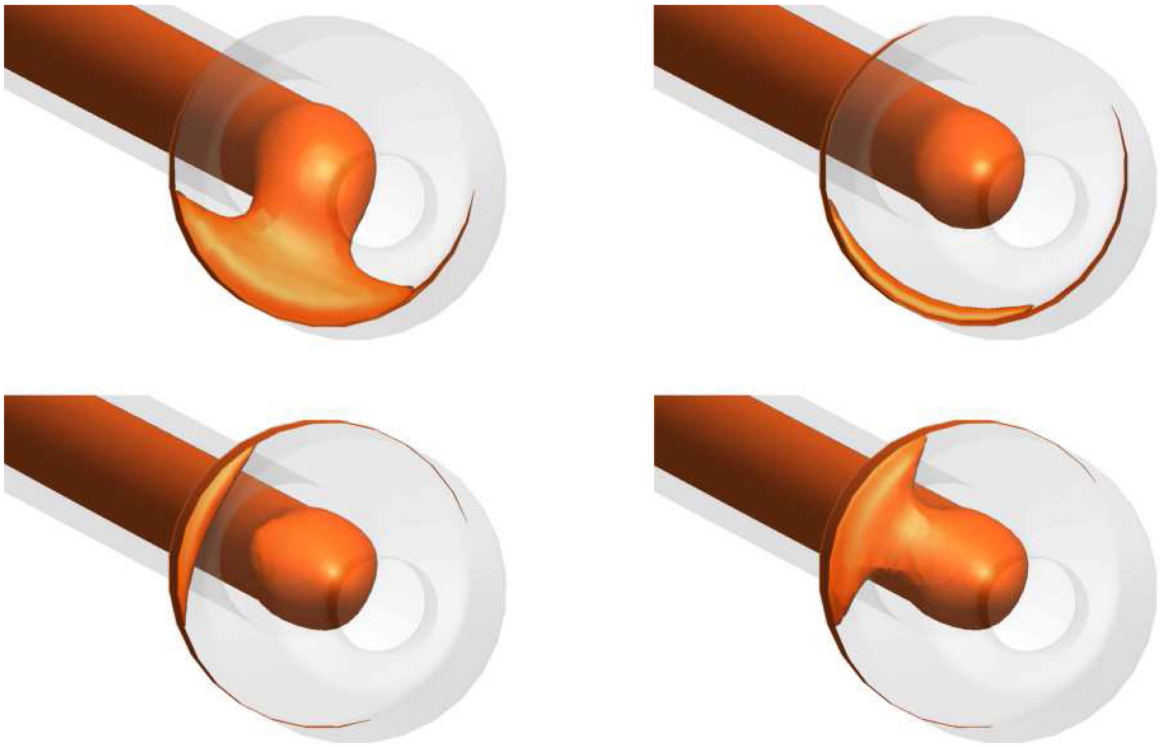

Figure 10. Formation of new attachment point: iso-surface for current density $J = 2.8 \times 10^5$ A m^{-2} at $t = 572.6$ μs (top-left), $t = 765.2$ μs (top-right), $t = 2140.2$ μs (bottom-left), and $t = 4540.2$ μs (bottom-right).

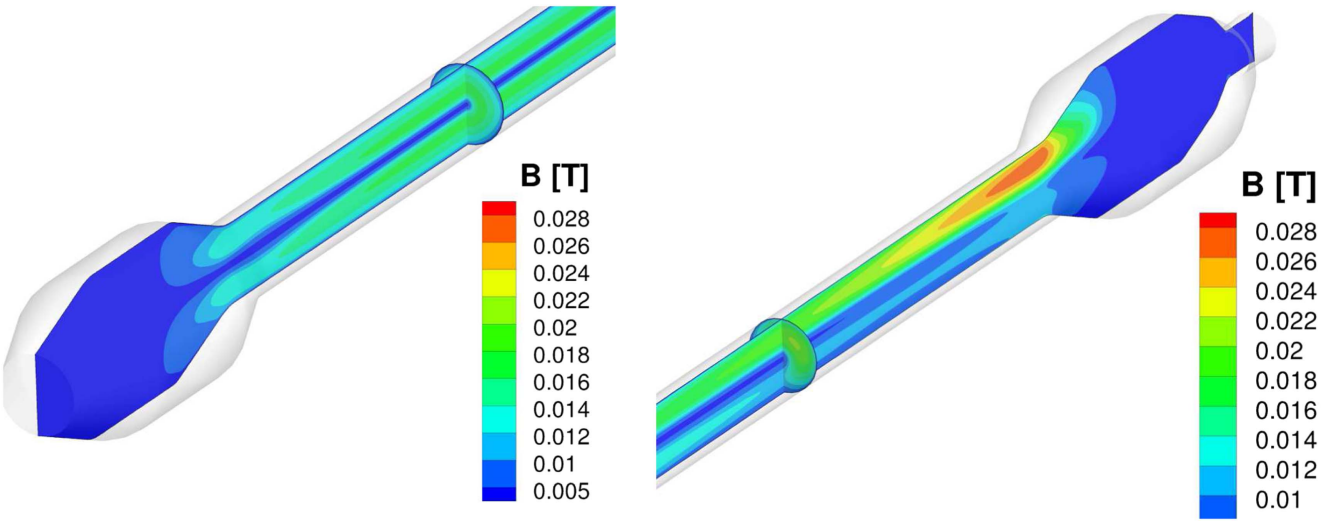

Figure 11. Magnitude of the induced magnetic field in the anode chamber (left), the constrictor, and the cathode chamber (right).

divergence of the radiative flux acts as a source term in the total and electro-vibrational energy equations, negative values indicate that emission is dominant over absorption and will result in a temperature decrease, while positive values indicate that the gas is absorbing radiation which will cause the temperature to increase. The high temperatures in the central region of the arc-column lead to strong emission of radiation, and to the subsequent gas-cooling effect. This is indicated by the contribution of radiative heating being negative around the centerline axis in figure 13. The radiation is then transported and absorbed in the colder regions closer to the walls. The overall consequence of these radiative transfer processes is a more uniformly heated flow entering the converging–diverging nozzle at the end of the arc heater. Figure 14 compares the Joule and radiative heating along the centerline axis. It is evident that although Joule heating dominates, radiative heat flux is a significant contributor to energy change in the flowfield and an

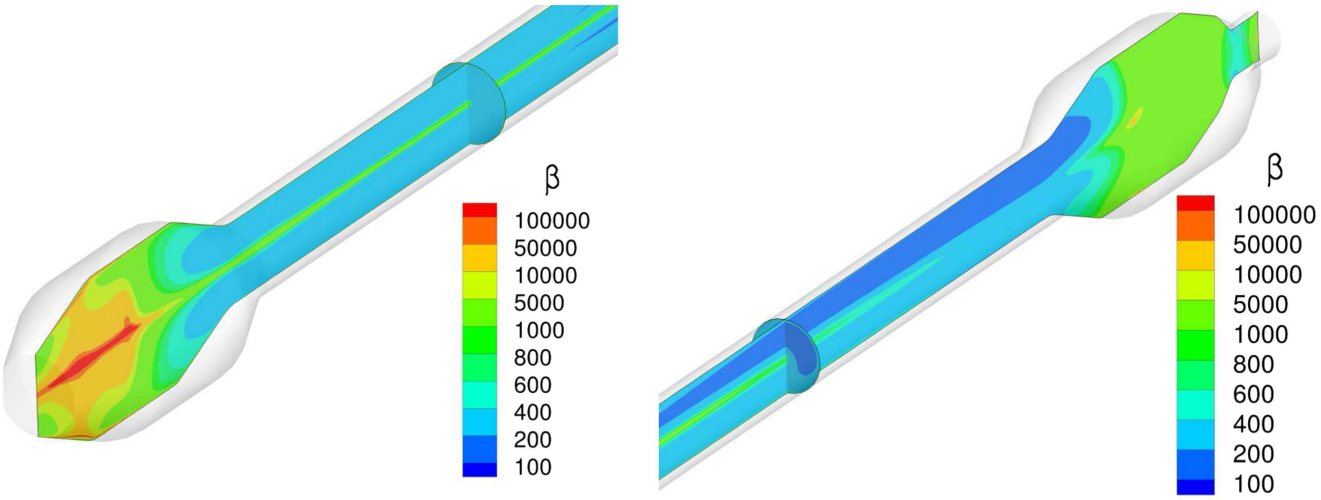

Figure 12. Distribution of the beta factor which represents the ratio of the hydrodynamic pressure to the magnetic pressure in the anode chamber (left), the constrictor, and the cathode chamber (right).

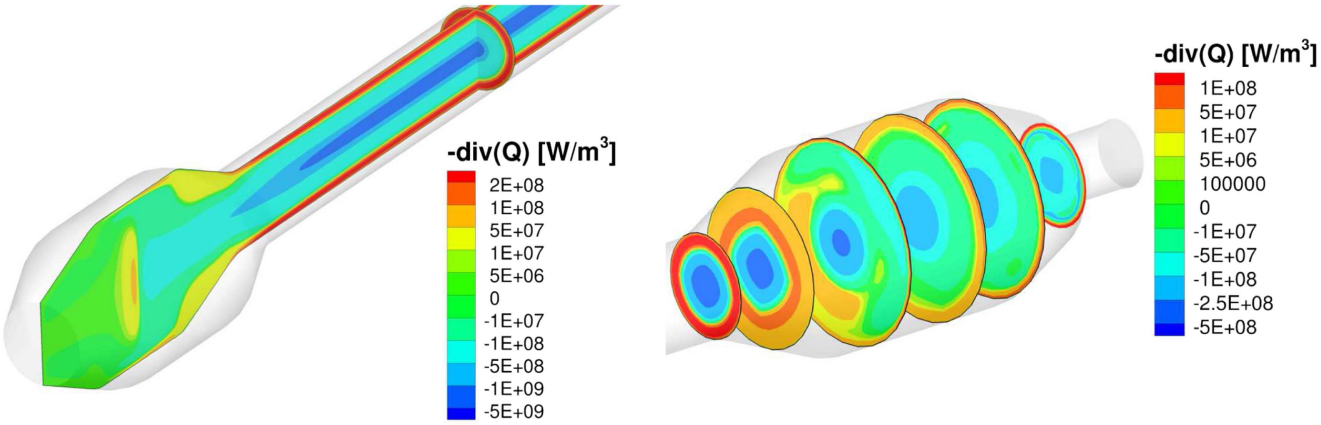

Figure 13. Radiative heating in the anode (left) and cathode (right) chamber.

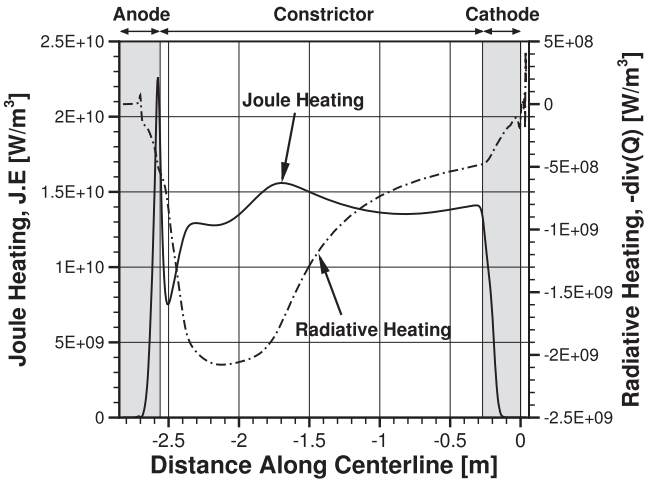

Figure 14. Joule and radiative heating along centerline axis.

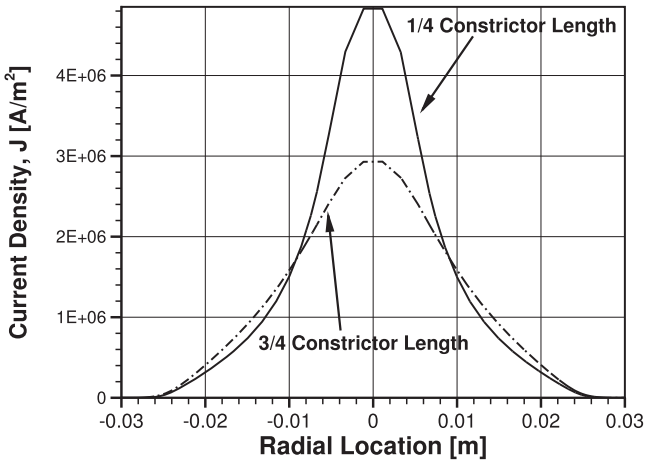

Figure 15. Current density along the horizontal plane at $1/4$ and $3/4$ of the constrictor length.

important heat transfer mechanism between the hot plasma core and the surrounding cool gas.

The impact of radiative energy exchange can be better understood by analyzing the radial distribution of properties at different locations on the constrictor. Figures 15–17 gives current density, Joule heating and temperatures along the horizontal plane at $1/4$ and $3/4$ of the constrictor length. The peak current density heating and temperatures decrease as the

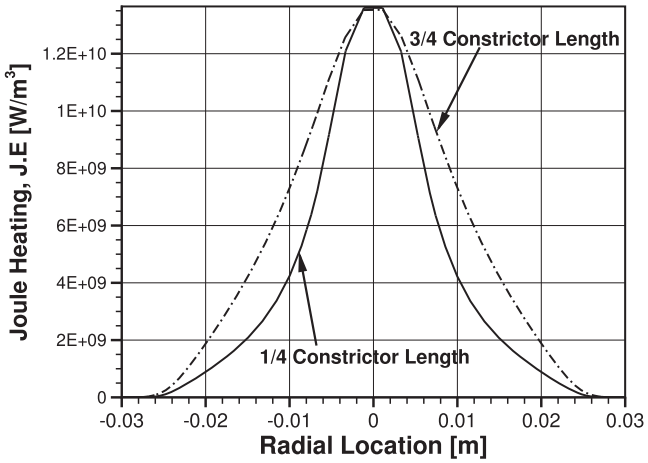

Figure 16. Joule heating along the horizontal plane at 1/4 and 3/4 of the constrictor length.

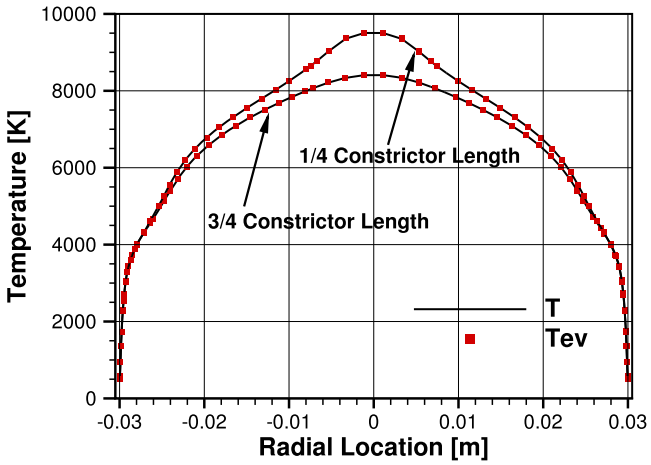

Figure 17. *Rotational-translational* temperature T and *electro-vibrational* temperature T_{ev} along the horizontal plane at 1/4 and 3/4 of the constrictor length.

flow moves downstream. However, the radial distribution curves broaden which indicates that the central arc column widens and the bulk of the total electric current flows through a larger cross-sectional area. The corresponding plot for Joule heating reflects this as well, with energy addition due to Joule heating becoming more even. The interplay between Joule heating and radiative heat transfer results in a more uniform flow at the end of the constrictor. The asymmetry induced by the arc-attachment also manifests in the distribution of the radiative heating term, and is especially pronounced in the cathode chamber (figure 13). This necessitates the use of a fully three-dimensional radiation code instead of a symmetry based solution strategy like cylindrical slab to accurately model the dynamics of the arc-jet.

The Reynolds number inside the AHF is of the order of 10^4, resulting in fully turbulent flow. Figure 18 present the distribution of the viscosity ratio, i.e. the turbulent eddy viscosity normalized by the local molecular viscosity in the AHF. The viscosity ratio is significantly greater than one for most of the flowfield which indicates that the contribution of turbulence to transport properties (viscosity, mass diffusivity, and thermal conductivity) is significant. Consequently, turbulence plays a crucial role in large facilities like the AHF and contributes to the heat flux between the hot core and cold flow near the wall. The formation of a vortex pair in the anode chamber due to axisymmetric mass injection induces turbulent mixing. This results in large local values for the viscosity ratio. The formation of vortices due to flow separation in the cathode also results in turbulent eddy viscosity dominating molecular viscosity. Turbulence appears to play a prominent role near the boundary between the hot core flow along the centerline and the cooler flow surrounding it. The effect of turbulence is also pronounced as the flow nears the throat because of the velocity increasing rapidly due to expansion in the nozzle section.

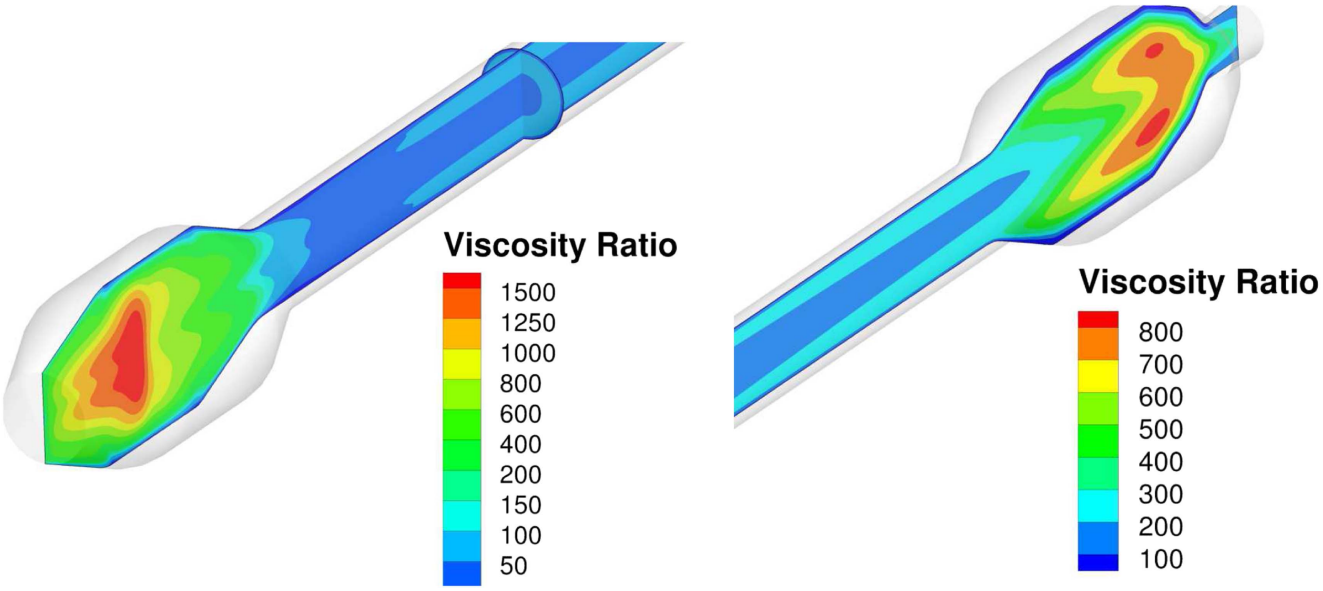

Figure 18. Ratio of turbulent eddy viscosity and local molecular viscosity in the anode chamber (left), the constrictor, and the cathode chamber (right) along the vertical plane.

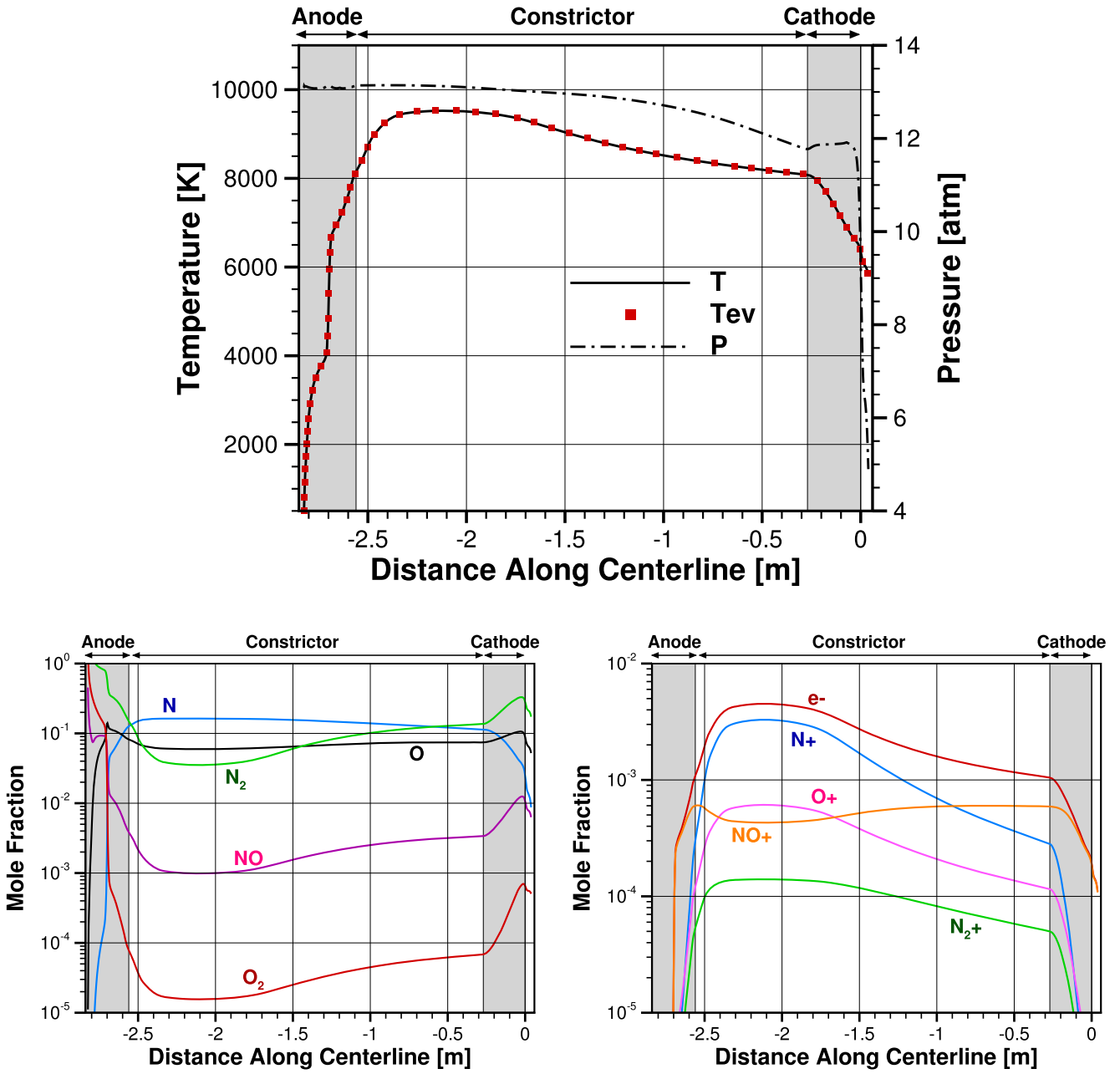

Figure 19. Property distribution along the centerline axis: temperature and pressure (top left), Joule and radiative heating (top right), and mole fraction of neutral (bottom left) and ionized (bottom right) species.

4.2.4. Thermo-chemical composition. The distribution of *rotational-translational* temperature, *electro-vibrational* temperature, total pressure, and species mole fractions along the centerline axis of the AHF is presented in figure 19. As expected, LTE is reached in the heater with $T = T_{ev}$. LTE is also observed in the radial distribution of temperatures presented in figure 17. The high pressure conditions inside the AHF result in a large number of collisions. This leads to fast energy exchanges among the energetic modes, rapidly bringing the gas towards a state of thermal equilibrium. Thus, as far as the current simulations are concerned, the use of a one-temperature model would have a negligible impact on the accuracy of the computed results. However, if a diverging nozzle were to be added to the domain, strong non-equilibrium effects would appear, necessitating the use of a two temperature model, as formulated in the present work, to accurately describe the system.

The two temperatures T and T_{ev} reach their peak values in the constrictor before the plasma starts cooling rapidly as it accelerates while traveling through the cathode chamber and the choked throat. The addition of large amounts of energy through Joule heating results in a chemically reactive flow. The axial distribution of species mole fractions indicates that molecular species undergo rapid dissociation and ionization at the exit of the anode chamber (figure 19). Ionization in the arc column results in the formation of free electrons which act as the primary current carriers for the electrical discharge between electrodes and result in high electric conductivity.

Thus, the arc is able to sustain itself by driving chemistry through Joule heating. A decrease in maximum observed temperatures in the downstream direction is evident from the radial distribution of T and T_{ev} at different locations along the constrictor (figure 17). This is due to a combination of energy re-distribution through radiation and heat loss at the walls. Consequently, the population of ionized and atomic species decreases gradually through the constrictor. Recombination reactions of atomic and ionized species become dominant downstream of the constrictor exit. However, the energy supplied by the re-formation of neutral molecular species to the internal energy modes is not enough to arrest the eventual drop in temperature due to the acceleration of the flow.

5. Conclusions

A simulation framework combining the robustness of an SUPG-type finite element flow solver with detailed models for the electric heating and radiation fields has been developed to provide a complete description of the multi-physics flow environment inside an arc-jet facility. The FIN-S code provides a time accurate solution of the FANS equations in chemical non-equilibrium. The SA one-equation model is used to close the RANS equations and simulate the effects of turbulent transport. The flowfield calculations have been loosely coupled to the electric and radiation field at every time step. A simplified electric field equation based on the generalized Ohm's law is solved to compute the contribution of the Joule heating term emanating from the applied current. The radiation transport equation has been solved using a finite element formulation of the discrete ordinate form with added streamwise diffusion to improve stability. Additionally, the present study builds upon previous results by employing a highly accurate multi-band reduced radiation model to accurately represent the highly non-gray spectral properties of high temperature air. Detailed simulations of plasma flows inside the complex AHF exhibit the capabilities of the current modeling approach. The newly developed framework is able to reproduce the fundamental characteristics of high enthalpy flows inside large arc-heaters—hot central core, asymmetry due to arc re-attachment, and supersonic expansion at exit. Energy addition due to Joule heating causes an increase in temperature and induces dissociation and ionization as the flow enters the constrictor. Heat loss and mass injection at the walls results in a hot central core which serves as a pathway for bulk of the applied electric current. Thermal radiation plays a key role re-distributing energy within the constrictor resulting in a more uniform flow. Turbulence is critical for such high Reynolds number flows with complex vortex structures and plays a key role in the diffusion of heat and momentum. The arc re-attachment process in the cathode chamber introduces strong time-dependent asymmetry, which is reflected in the distribution of all flow variables. Recombination reactions start occurring downstream of the constrictor exit. The flow begins to accelerates as it heads towards the throat and becomes supersonic at the domain outlet.

The next step in this research is validation using experimental data for bulk properties like arc voltage, total enthalpy, and pressure and detailed parametric analysis. These studies coupled with improved formulations for magnetic forces and electrode sheath behavior would allow predictive simulations of the operating characteristics of these high-enthalpy arc-jet facilities. The current framework can be used to model a whole spectrum of flow problems ranging from hypersonic planetary entry to ground-based arc heated wind-tunnel testing [49]. This versatility allows test conditions to be devised for given flight conditions and conversely interpret experimental data to further refine the vehicle design process.

Acknowledgments

The support from the NASA Johnson Space Center (JSC) is gratefully acknowledged (Grant # NNX13AN62A). Dr Panesi's research is also supported by the AE Multidisciplinary Initiative, Department of Aerospace Engineering, University of Illinois at Urbana-Champaign. The authors would like to thank Dr BS Kirk (NASA JSC) and Dr R Stogner (University of Texas at Austin) for the helpful discussion and for providing access to LIBMESH library and FIN-S solver.

References

[1] Driver D M *et al* 2014 Arcjet testing in shear environment for Mars science laboratory thermal protection system *J. Spacecr. Rockets* **51** 1151–66

[2] Mark Hightower T, MacDonald C L, Martinez E R, Balboni J A and Anderson K F 2002 Enthalpy by energy balance for aerodynamic heating facility at NASA Ames research center arc jet complex *Proc. Int. Instrumentation Symp.* vol 48, pp 117–29 https://ntrs.nasa.gov/search.jsp?R=20020062996

[3] Sakai T and Olejniczak J 2003 Improvements in a Navier–Stokes code for arc heater flows *AIAA Paper* **vol 3782**

[4] Sakai T, Sawada K and Mitsuda M 2001 Application of Planck–Rosseland–Gray model for high-enthalpy arc heaters *J. Thermophys. Heat Transfer* **15** 176–83

[5] Sakai T 2007 Computational simulation of high enthalpy arc heater flows *J. Thermophys. Heat Transfer* **21** 77–85

[6] Lee J I, Kim C and Kim K H 2007 Accurate computations of arc-heater flows using two-equation turbulence models *J. Thermophys. Heat Transfer* **21** 67–76

[7] Matsuzaki T, Ishida K, Watanabe Y, Miho K, Itagaki H and Yoshinaka T 2001 *Constructions and Characteristics of the 750 kW Arc Heated Wind Tunnel* NAL TM-760 National Aerospace Laboratory, Chofu, Japan https://repository.exst.jaxa.jp/dspace/handle/a-is/36741

[8] Takahashi Y, Kihara H and Abe Ki 2010 Numerical investigation of nonequilibrium plasma flows in constrictor- and segmented-type arc heaters *J. Thermophys. Heat Transfer* **24** 31–9

[9] Takahashi Y, Kihara H and Abe Ki 2010 The effects of radiative heat transfer in arc-heated nonequilibrium flow simulation *J. Phys. D: Appl. Phys.* **43** 185201

[10] Takahashi Y, Kihara H and ichi Abe K 2011 Turbulence and radiation behaviours in large-scale arc heaters *J. Phys. D: Appl. Phys.* **44** 085203

[11] Takahashi Y, Abe T, Takayanagi H, Mizuno M, Kihara H and Abe Ki 2014 Advanced validation of nonequilibrium plasma flow simulation for arc-heated wind tunnels *J. Thermophys. Heat Transfer* **28** 9–17

[12] Trelles J P and Modirkhazeni S M 2014 Variational multiscale method for nonequilibrium plasma flows *Comput. Methods Appl. Mech. Eng.* **282** 87–131

[13] Trelles J 2013 Flow dynamics from a nonequilibrium atmospheric-pressure arc discharge jet *APS Meeting Abstracts* vol 1, p 1039 http://faculty.uml.edu/Juan_Pablo_Trelles/Publications/documents/Trelles_Flow_Dynamics_from_a_Nonequilibrium_Atmospheric-Pressure_Arc_Discharge_Jet_2013.pdf

[14] Trelles J P, Chazelas C, Vardelle A and Heberlein J V R 2009 Arc plasma torch modeling *J. Therm. Spray Technol.* **18** 728–52

[15] Trelles J P, Pfender E and Heberlein J 2006 Multiscale finite element modeling of arc dynamics in a DC plasma torch *Plasma Chem. Plasma Process.* **26** 557–75

[16] Terrazas-Salinas I and Cornelison C 2009 *Test Planning Guide for Nasa Ames Research Center Arc Jet Complex and Range Complex, Space Technology Division* 4 A029-9701-XM3 Rev. C NASA Ames Research Center, Moffett Field, CA 94035 www.nasa.gov/sites/default/files/testplanningguiderevc.pdf

[17] Kirk B S 2007 Adaptive finite element simulation of flow and transport applications on parallel computers *PhD Thesis* The University of Texas at Austin http://hdl.handle.net/2152/13302

[18] Kirk B S, Stogner R H, Oliver T A and Bauman P T 2013 Recent advancements in fully implicit numerical methods for hypersonic reacting flows *AIAA Paper* **vol 2559**

[19] Kirk B S, Peterson J W, Stogner R H and Carey G F 2006 LibMesh: a C++ library for parallel adaptive mesh refinement/coarsening simulations *Eng. Comput.* **22** 237–54

[20] Munafò A, Lani A, Bultel A and Panesi M 2013 Modeling of non-equilibrium phenomena in expanding flows by means of a collisional-radiative model *Phys. Plasmas* **20** 073501

[21] Munafò A, Liu Y and Panesi M 2015 Modeling of dissociation and energy transfer in shock-heated nitrogen flows *Phys. Fluids* **27** 127101

[22] Liu Y, Panesi M, Sahai A and Vinokur M 2015 General multi-group macroscopic modeling for thermo-chemical non-equilibrium gas mixtures *J. Chem. Phys.* **142** 134109

[23] Gnoffo P A 1999 Planetary-entry gas dynamics *Annu. Rev. Fluid Mech.* **31** 459–94

[24] Park C 1993 Review of chemical-kinetic problems of future NASA missions: I. Earth entries *J. Thermophys. Heat Transfer* **7** 385–98

[25] Gnoffo P A, Gupta R N and Shinn J L 1989 *Conservation Quations and Physical Models for Hypersonic Air Flows in Thermal and Chemical Non-Equilibrium* No. 2867 NASA https://ntrs.nasa.gov/search.jsp?R=19890006744

[26] Bottin B, Vanden Abeele D, Carbonaro M, Degrez G and Sarma G S R 1999 Thermodynamic and transport properties for inductive plasma modeling *J. Thermophys. Heat Transfer* **13** 343–50

[27] Hirschfelder J O, Curtiss C F, Bird R B and Mayer M G 1954 *Molecular Theory of Gases and Liquids* vol 26 (New York: Wiley)

[28] Zhdanov V M and Tirskiy G A 2007 A phenomenological and kinetic description of diffusion and heat transport in multicomponent gas mixtures and plasma *J. Appl. Math. Mech.* **71** 718–36

[29] Giovangigli V 2010 Multicomponent transport algorithms for partially ionized mixtures *J. Comput. Phys.* **229** 4117–42

[30] Liu L H and Tan H P 2004 Transient temperature response in semitransparent variable refractive index medium subjected to a pulse irradiation *J. Quant. Spectrosc. Radiat. Transfer* **83** 333–44

[31] Wray A A, Bensassi K, Kitiashvili I N, Mansour N N and Kosovichev A G 2015 Simulations of stellar magnetoconvection using the radiative MHD code 'StellarBox' arXiv:150707999

[32] McClarren R G and Urbatsch T J 2009 A modified implicit Monte Carlo method for time-dependent radiative transfer with adaptive material coupling *J. Comput. Phys.* **228** 5669–86

[33] Sohn I, Li Z, Levin D A and Modest M F 2012 Coupled DSMC-PMC radiation simulations of a hypersonic reentry *J. Thermophys. Heat Transfer* **26** 22–35

[34] Coelho P J 2002 Bounded skew high-order resolution schemes for the discrete ordinates method *J. Comput. Phys.* **175** 412–37

[35] Murthy J Y and Mathur S R 1998 Finite volume method for radiative heat transfer using unstructured meshes *J. Thermophys. Heat Transfer* **12** 313–21

[36] Castro R O and Trelles J P 2015 Spatial and angular finite element method for radiative transfer in participating media *J. Quant. Spectrosc. Radiat. Transfer* **157** 81–105

[37] Abe Ki, Kameyama T, Kihara H, Nishida M, Ito K and Tanno H 2005 Computation and experiment of a nonequilibrium nozzle flow of arc-heated air *J. Thermophys. Heat Transfer* **19** 428–34

[38] Hirata N, Yamada M, Kihara H, Abe Ki and Takahashi Y 2014 Improvement of a three-band radiation model for application to chemical nonequilibrium flows *J. Thermophys. Heat Transfer* **28** 799–803

[39] Modest M F 2003 Narrow-band and full-spectrum k-distributions for radiative heat transfercorrelated-k versus scaling approximation *J. Quant. Spectrosc. Radiat. Transfer* **76** 69–83

[40] Bansal A, Modest M F and Levin D A 2011 Multi-scale k-distribution model for gas mixtures in hypersonic nonequilibrium flows *J. Quant. Spectrosc. Radiat. Transfer* **112** 1213–21

[41] Salah N B, Soulaimani A, Habashi W G and Fortin M 1999 A conservative stabilized finite element method for the magneto-hydrodynamic equations *Int. J. Numer. Methods Fluids* **29** 535–54

[42] Trelles J P 2016 Finite element methods for arc discharge simulation *Plasma Process. Polym.* at press (https://doi.org/10.1002/ppap.201600092)

[43] Gurvich L V, Veyts I V and Alcock C B 1989 *Thermodynamic Properties of Individual Substances* (New York: Hemisphere) p 1

[44] Park C, Jaffe R L and Partridge H 2001 Chemical-kinetic parameters of hyperbolic Earth entry *J. Thermophys. Heat Transfer* **15** 76–90

[45] Park C 1989 Assessment of two-temperature kinetic model for ionizing air *J. Thermophys. Heat Transfer* **3** 233–44

[46] Scoggins J B and Magin T E 2014 Development of mutation++: multicomponent thermodynamics and transport properties for ionized gases library in C++ *AIAA Paper* **vol 2966**

[47] Gupta R N, Yos J M, Thompson R A and Lee K P 1990 *A Review of Reaction Rates and Thermodynamic and Transport Properties for an 11-species Air Model for Chemical and Thermal Non-Equilibrium Calculations to 30 000 K* No. 1232 NASA https://ntrs.nasa.gov/search.jsp?R=19900017748

[48] Devoto R S 1976 Electron transport properties in high-temperature air *Phys. Fluids* **19** 22–4

[49] Sahai A 2015 Modeling of high enthalpy flows for hypersonic re-entry and ground-based arc-jet testing *Master's Thesis* University of Illinois at Urbana-Champaign http://hdl.handle.net/2142/78575
[50] Degrez G, Lani A, Panesi M, Chazot O and Deconinck H 2009 Modelling of highenthalpy, high-mach number flows *J. Phys. D: Appl. Phys.* **42** 194004
[51] Panesi M, Rini P, Degrez G and Chazot O 2007 Analysis of chemical nonequilibrium and elemental demixing in plasmatron facility *J. Thermophys. Heat Transfer* **21** 57–66
[52] Munafò A, Alfuhaid S, Cambier J L and Panesi M 2015 A tightly coupled non-equilibrium model for inductively coupled radio-frequency plasmas *J. Appl. Phys.* **118** 133303
[53] Zhang W, Lani A and Panesi M 2016 Analysis of non-equilibrium phenomena in inductively coupled plasma generators *Phys. Plasmas* **23** 073512
[54] Spalart P R and Allmaras S R 1992 A one-equation turbulence model for aerodynamic flows *AIAA Paper* AIAA-92-0439 (https://doi.org/10.2514/6.1992-439)
[55] Kirk B S and Carey G F 2008 Development and validation of a SUPG finite element scheme for the compressible navier-stokes equations using a modified inviscid flux discretization *Int. J. Numer. Methods Fluids* **57** 265–93
[56] Kirk B S, Stogner R H, Bauman P T and Oliver T A 2014 Modeling hypersonic entry with the fully-implicit Navier–Stokes (FIN-S) stabilized finite element flow solver *Comput. Fluids* **92** 281–92
[57] Erwin J T, Anderson W K, Kapadia S and Wang L 2013 Three-dimensional stabilized finite elements for compressible navier-stokes *AIAA J.* **51** 1404–19
[58] Guennebaud G *et al* 2010 Eigen v3 http://eigen.tuxfamily.org
[59] Kirk B S, Bova S W and Bond R B 2011 A streamline-upwind Petrov–Galerkin finite element scheme for non-ionized hypersonic flows in thermochemical nonequilibrium *AIAA Paper 2011* **vol 134**
[60] Shakib F, Hughes T J R and Johan Z 1991 A new finite element formulation for computational fluid dynamics: X. The compressible Euler and Navier–Stokes equations *Comput. Methods Appl. Mech. Eng.* **89** 141–219
[61] Baudry C, Vardelle A, Mariaux G, Abbaoui M and Lefort A 2005 Numerical modeling of a DC non-transferred plasma torch: movement of the arc anode attachment and resulting anode erosion *High Temp. Mater. Process.: Int. Q. High-Technol. Plasma Process.* **9** 1–15
[62] Trelles J P 2007 Finite element modeling of flow instabilities in arc plasma torches *PhD Thesis* University of Minnesota
[63] Balay S *et al* 2016 *PETSc Users Manual* ANL-95/11 Revision 3.7Argonne National Laboratory
[64] Barrett R *et al* 1994 *Templates for the Solution of Linear Systems: Building Blocks for Iterative Methods* vol 43 (Philadelphia: SIAM)
[65] Golub G H and Van Loan C F 1989 *Matrix Computations* (*Johns Hopkins Series in the Mathematical Sciences*) (Baltimore, MD: Johns Hopkins University Press)
[66] Karypis G and Kumar V 1995 *Metis-Unstructured Graph Partitioning and Sparse Matrix Ordering System, Version 2.0* Department of Computer Science, University of Minnesota http://dm.kaist.ac.kr/kse625/resources/metis.pdf
[67] Edén M and Levitt M H 1998 Computation of orientational averages in solid-state NMR by Gaussian spherical quadrature *J. Magn. Reson.* **132** 220–39
[68] Gander M J and Karp A H 2001 Stable computation of high order Gauss quadrature rules using discretization for measures in radiation transfer *J. Quant. Spectrosc. Radiat. Transfer* **68** 213–23
[69] Liu L H 2007 Least-squares finite element method for radiation heat transfer in graded index medium *J. Quant. Spectrosc. Radiat. Transfer* **103** 536–44
[70] Richling S, Meinköhn E, Kryzhevoi N and Kanschat G 2001 Radiative transfer with finite elements: I. Basic method and tests *Astron. Astrophys.* **380** 776–88
[71] Tarvainen T, Vauhkonen M and Arridge S R 2008 Gauss–Newton reconstruction method for optical tomography using the finite element solution of the radiative transfer equation *J. Quant. Spectrosc. Radiat. Transfer* **109** 2767–78
[72] Scoggins J B, Magin T, Wray A and Mansour N N 2013 Multi-group reductions of LTE air plasma radiative transfer in cylindrical geometries *44th AIAA Thermophysics Conf.* **vol 3142**
[73] Whiting E E, Park C, Liu Y, Arnold J O and Paterson J A 1996 *NEQAIR96, Nonequilibrium and Equilibrium Radiative Transport and Spectra Program: User's Manual* NASA-RP-1389 https://ntrs.nasa.gov/search.jsp?R=19970004690&qs=N%3D4294966753%2B4294967219%26No%3D60%26Nn%3D4294965552%257CSubject%2BTerms%257CSIMULATION
[74] Malaya N, Estacio-Hiroms K C, Stogner R H, Schulz K W, Bauman P T and Carey G F 2013 MASA: a library for verification using manufactured and analytical solutions *Eng. Comput.* **29** 487–96
[75] Oliver T A, Estacio-Hiroms K C, Malaya N and Carey G F 2012 Manufactured solutions for the favre-averaged Navier–Stokes equations with eddy-viscosity turbulence models *AIAA Paper* AIAA-92-0439 (https://doi.org/10.2514/6.2012-80)
[76] Mckeon B J, Li J d, Jiang W, Morrison J F and Smits A J 2004 Further observations on the mean velocity distribution in fully developed pipe flow *J. Fluid Mech.* **501** 135–47
[77] Modest M F 2013 *Radiative Heat Transfer* (New York: Academic)
[78] Trelles J and Heberlein J 2006 Simulation results of arc behavior in different plasma spray torches *J. Therm. Spray Technol.* **15** 563–9
[79] Freidberg J P 1987 *Ideal Magnetohydrodynamics* (New York: Plenum)
[80] Geister D 1969 A high pressure AC arc heater system *AIAA Paper* p 348